scientific reports



OPEN

Development of a fixed-order H_{∞} controller for a robust P&O-MPPT strategy to control poly-crystalline solar PV energy systems

Moussa Sedraoui^{1⊠}, Mohcene Bechouat², Ramazan Ayaz³,⁴, Yahya Z. Alharthi⁵, Abdelhalim Borni⁶, Layachi Zaghba⁶, Salah K. ElSayed⁵, Yayehyirad Ayalew Awoke^{8⊠} & Sherif S. M. Ghoneim⁵

This paper presents a novel approach to modeling and controlling a solar photovoltaic conversion system(SPCS) that operates under real-time weather conditions. The primary contribution is the introduction of an uncertain model, which has not been published before, simulating the SPCS's actual functioning. The proposed robust control strategy involves two stages: first, modifying the standard Perturb and Observe (P&O) algorithm to generate an optimal reference voltage using real-time measurements of temperature, solar irradiance, and wind speed. This modification leads to determining and linearizing the nonlinear current-voltage (I-V) characteristics of the photovoltaic (PV) array near standard test conditions (STC), resulting in an uncertain equivalent resistance used to synthesize an overall model. In the second stage, a robust fixed-order H_{∞} controller is designed based on this uncertain model, with frequency-domain specifications framed as a weighted-mixed sensitivity problem. The optimal solution provides the controller parameters, ensuring good reference tracking dynamics, noise suppression, and attenuation of model uncertainties. Performance assessments at STC compare the standard and robust P&O-MPPT strategies, demonstrating the proposed method's superiority in performance and robustness, especially under sudden meteorological changes and varying loads. Experiment results confirm the new control strategy's effectiveness over the standard approach.

In most industrial applications, the real-time implementation of existing controllers is confronted with numerous failures, leading to lost time, reduced productivity, and high cost of repairs. These malfunctions are generally due to non-precise computation concerning the parameters of the synthesized controller. For instance, when designing a PID controller, it is essential to fine-tune its three gains—the proportional gain, the integral gain, and the derivative gain - while meeting all the designer's requirements. It requires the proper settings, of which the availability of a correct mathematical model is one of the main requirements. Unfortunately, a perfect model is rarely available for most industrial applications. It is due to several factors, such as the necessity of linearizing the dynamics of the controlled system, the necessity of neglecting some unmodeled high-frequency modes when providing the simplified linear model, and so on². Consequently, all these challenges require prior acknowledgment of all possible uncertainties that may affect the synthesized model, which in turn requires the design of a robust controller that must be synthesized using one of the strategies based on robust control theory.

¹Department of Electrical and Automation Engineering, Faculty of Science and Technology, University of 08 mai 1945 Guelma, Guelma, Algeria. ²Département d'Automatique et d'électromécanique, Facult é des sciences et de la technologie, Université de Ghardaia, Ghardaia, Algeria. ³Department of Electrical Engineering, Davutpasa Campus, Yildiz Technical University, Istanbul 34220, Turkey. ⁴Clean Energy Technologies Institute, Davutpasa Campus, Yildiz Technical University, Istanbul 34220, Turkey. ⁵Department of Electrical Engineering, College of Engineering, University of Hafr Albatin, Hafr Al Batin 39524, Saudi Arabia. ⁶Untié de Recherche Aplliquée en Energies Renouvlables, URAER, Centre de Déveloopement des Energies Renouvlables, CDER, 47133 Ghardaia, Algeria. ⁷Department of Electrical Engineering, College of Engineering, Taif University, Taif 21944, Saudi Arabia. ⁸Department of Electrical and Computer Engineering, Debre Markos Institute of Technology, Debre Markos University, Taif 21944, Saudi Arabia. [∞]Department of Electrical Engineering, College of Engineering, Taif University, Taif University, Taif 21944, Saudi Arabia. [∞]Department of Electrical Engineering, College of Engineering, Taif University, Taif 21944, Saudi Arabia. [∞]Department of Electrical Engineering, College of Engineering, Taif University, Taif 21944, Saudi Arabia.

It should be noted here that the synthesis of such robust controllers requires prior consideration of all model uncertainties, which are due to an inadequate choice of model structure for correctly describing the actual behavior of the system, or to an erroneous choice of identification technique that guarantees a precise computation of model parameters. Moreover, it is important to carry out a rigorous assessment of all exogenous effects having a direct or indirect impact on the control chain, such as the effects of sensor noise in the event of transducer malfunction, the effect of environmental disturbances, etc³. In fact, by fully identifying all these unavoidable effects, it is possible to define a robustness condition, called robust stability RS. This condition must be satisfied throughout the frequency range, especially if the synthesized model is subject to unknown uncertainties⁴. This allows to secure the closed-loop system with an increasingly high safety margin. At the same time, satisfying the RS condition is not enough when designing the desired robust controller, as there is another condition whose role is totally complementary to the previous one, requiring it to be satisfied in the same frequency range. It is known as nominal performance NP⁴. It often includes all the necessary proprieties to reach the desired reference tracking dynamics. Such properties include the overshoot of the time response of the closed-loop system, the steady-state error, the two rise and settling times given in the transient state, and so on.⁴.

Besides, meeting the two preceding conflicting objectives together becomes quite impossible in the same frequency range, where finding a trade-off between them presents a real challenge for most designers of robust controllers. Note that meeting the RS condition becomes more crucial, especially in high frequencies while meeting the NP condition becomes crucial, especially in low frequencies. So, in terms of sensitivity functions, the ideal shape corresponding to the plot of the maximal singular values of the direct sensitivity reflecting the desired NP needs to be minimized, as far as possible, at low frequencies and to approach the unity value at high frequencies⁵. Conversely, the ideal shape corresponding to the plot of the maximal singular values of the complementary sensitivity reflecting the desired RS needs to be minimized, as far as possible, at high frequencies and to approach the unity value at low frequencies. This results in each frequency point obtaining the value of unity when summing the maximal singular values of the two plots corresponding to the direct and complementary sensitivity functions^{5,6}. Later, we see that the margin of the trade-off, ensured by different robust controllers, can be compared by measuring the distance provided by the unit value and the sum of two previous sensitivity functions that correspond to each controller.

In the engineering of SPCS, it is obvious that the design of a robust controller is often better achieved when the actual behavior of the SPCS is based on an uncertain model. This is due to several reasons, such as the existence of non-linearity in the I-V characteristic of the overall PV model, whose parameters often vary over time as a function of unpredictable changes in weather conditions. Consequently, such a PV model having fixed parameters may not accurately reflect the actual behavior of the SPCS when facing a sudden change in weather conditions. However, uncertain models appear to be closer to reality. This reasoning becomes true not only in the case of SPCS functioning in the STC but also where real-time measurements of weather conditions are considered. In addition, it is possible to linearize the actual behavior of the SPCS by applying the small-signal principle. It is based on the elimination of all steady-state variations of the electrical variables, as well as those whose variation exceeds strictly the order of one. In any case, uncertain models seem to be more able to cover all possible modeling errors, thus providing a fairly correct synthesis of the robust controller using one of the MPPT strategies.

The control strategy to be implemented in this paper consists of two cascaded control loops⁹. The first loop consists of using the modified P&O algorithm instead of the standard one. The main aim is to generate an optimal reference voltage output as a function of variations in real-time measurements of total PV power input and total PV voltage input where the last one is measured at the terminals of the overall PV array based on a series connection of four PV panels of poly-crystalline technology. As a starting stage, the modified P&O algorithm must be initialized with an initial reference voltage that corresponds to an initial position of the MPP. When one or more climatic conditions vary uniformly or randomly, a new unknown MPP position is produced. In this case, the previous voltage is updated by a fixed step until reaching its optimal value that corresponds to a new MPP position. Here, the resulting optimal reference voltage is considered as a set-point input, to be followed in the second control loop using the robust voltage controller^{10,11}.

The second loop consists of updating an initial duty cycle control by minimizing a voltage error, that occurred at each sampling time. This last one is generated when the optimal reference voltage input is compared by the measured total PV voltage of the preceding overall PV array. It is therefore a case of cascade control of the total PV power, in which its threshold must always be reached. For the SPCS, the input variables correspond to the three preceding climatic conditions, and the output variable corresponds to the total power. This last one must be generated with a ripple-free to avoid affecting the sustainability of each component in the SPCS. The control variable to be optimally generated consists of defining a favorable duty cycle, to guarantee the most precise possible setting of the switching frequency in the DC-DC boost converter. Based on previous research focusing on the two-stage P&O -MPPT strategy, the latter is not a new design for SPCS control. Rather, the novelty resides in the type of overall model used in its second loop to design a desired robust controller. It also lies in meeting the designer's pre-imposed requirements.

Knowing that the desired overall model of the SPCS includes another auxiliary model simulating the functioning of the PV array at STC. This model is designed through an equivalent electrical circuit including some unknown components, such as the diode ideality factor, series resistance, and shunt resistance where the value of each one can be optimized using an appropriate optimization tool¹¹. Next, the I-V characteristic resulting from this model is linearized at STC. It enables the determination of the two new electrical components, called also: nominal equivalent resistance and nominal equivalent voltage source. Thanks to the preceding linearization step, the linear relationship between the nominal total current and nominal total voltage is established, later used in the next step¹⁰. Next, the nonlinear state-space representation describing the functioning of the SPCS is established. Its linearization step is carried out by applying the small-signal principle, in which the previous

linear relationship is used. This leads to building the overall linear small-signal model, by which the parameters of the desired controller can be set using some guidelines available in the literature. Following these procedures leads to improving the performance of the preceding strategy. Accordingly, some researchers have recently synthesized some efficient controllers by employing this kind of overall linear small-signal model.

Among them, Aissani et al., (2023) used the Simulink-MATLAB software, including a graphical user interface (GUI) to design the overall linear small-signal model. It is used to set the parameters of the PID controller using the loop shaping principle, combined with the frequency identification technique¹². In the same year, Tadj et al., (2023) designed the fractional-order PID controller, i.e., FO-PID, using the Aquila optimizer¹³. One year later, Refaat et al., (2024) optimized the parameters of the controller using horse herd optimization¹⁴. In a parallel project, Bechouat et al., (2024) developed a linear small-signal model based on experimental input-output data, collected as frequency data using a free Piecewise Linear Electrical Circuit Simulation (PLECS) software. The resulting overall small-signal model was then employed to tune the parameters of the PID controller using *Pidtune* function of MATLAB software. This controller was implemented to improve the performance of the incremental conductance INC-MPPT strategy¹⁵. All these two-stage P&O -MPPT strategies have demonstrated their relevance and cost-effectiveness in terms of extracting as much as possible electrical energy from solar energy conversion systems. Nevertheless, the key to success still depended on guaranteeing a very high level of accuracy in the modeling of the small-signal linear model.

Compared to all these recent synthesis methods used in the same context, the main contribution lies in the design of an uncertain small-signal model and in quantifying all plant uncertainties to highlight the robustness conditions to be met. These conditions are then formulated in the form of a weighted mixed sensitivity problem, whose solution enables to design of the appropriate robust controller.

Following the above-mentioned introduction, the remaining sections will be organized as follows. Second section is devoted to describing the control loop used to achieve a maximal extraction of energy from the SPCS. Also, it explains how to optimize the three key parameters of the equivalent electrical circuit of the PV model using GA. It then follows with the linearization of the I-V characteristic of the PV model at the STC, which allows determining the nominal value of the equivalent linearization resistances as well as the set of uncertain ones. In addition, this section aims to determine the uncertain linear representation of the state space representation describing the functioning of the SPCS using the small signal principle. Third section describes in detail the design of the robust fixed-order H_{∞} controller where the synthesis problem is formulated as a weighted mixed sensitivity problem, whose optimal solution provides the desired controller for which a trade-off between performance and robustness must be ensured. The fourth section describes the experimental test including the real-time measurements. Some of them are used for the PV design model, other measurements are used to validate the PV model and some other measurements are used to evaluate the performance of the SPCS. The document ends with a general conclusion (fifth section), in which further avenues of work are suggested.

The control loop used for the maximal power extraction of the SPCS

The SPCS to be controlled is often operated under three climatic conditions that change in real-time, such as outdoor temperature, solar irradiation, and wind speed. Accordingly, a perfect extraction of the maximal power is usually ensured in STC, in which the nominal temperature is given by T_{stc} refers to the ambient temperature with the nominal value of $25^{\circ}C$ and the nominal solar irradiance is given by $G_{stc}=1000W/m^2$. The corresponding nominal MPP position must be closely tracked using appropriate control strategies, where performances resulting from one can be evaluated in STC. As this position is heavily dependent on the variation of one or more of the preceding meteorological conditions, it must be supervised and tracked according to specific requirements. In this paper, the robust P&O-MPPT strategy will be detailed and its performances will be compared with the ones resulting from the same kind of control strategy. To begin, let's consider the control loop of the SPCS, controlled by the proposed robust P&O-MPPT strategy (see Fig. 1).

It consists of a set of PV panels based on poly-crystalline technology. It is used as a PV generator to feed a variable resistive load throughout a DC-DC boost converter. Here, the PV generator has N_s number of seriesconnected PV panels per string. It also contains N_p number of parallel strings, giving the total current I_{pv}^g and the total voltage V_{pv}^g , where $I_{pv}^g = N_p \cdot I_{pv}^1$ and $V_{pv}^g = N_s \cdot V_{pv}^1$. Moreover, I_{pv}^1 and V_{pv}^1 are the current and the voltage corresponding one PV panel. In general, the total electrical power P_{pv}^g , generated by the PV array, is defined by $P_{pv}^g = I_{pv}^g \cdot V_{pv}^{g-12}$.

As mentioned before, the control loop is ensured by the 2-stages P&O-MPPT strategy. In the first stage, the optimal reference voltage V_{ref}^{opt} , carried out the modified P&O algorithm block, is generated, which defining both the new MPP position to be tracked, as well as, the new threshold of the total electrical power P_{pv}^g to be extracted in event of changes in real-time measurements of the three preceding climatic conditions. Further details of the modified P&O algorithm can be found in Appendix A¹⁵⁻¹⁷. In the second stage, the reference voltage V_{ref}^{opt} is compared by the measured total voltage V_{pv}^g , providing the total voltage error δe_v at each sampling time k. This last one must be attenuated, as much as possible, by the robust fixed-order H_{∞} controller to provide the optimal variation $\delta D(t)$ of the duty cycle control D(t), which usually initialized by the corresponding STC value It is assumed that the SPCS to be used for the generation of the global PV power will be operated in the STC. It is composed of three electrical devices that are connected in series according to the following order: Solar generator, DC-DC boost converter, and variable resistive load R. (see Fig. 1).

According Fig. 1, it is clear to see that the optimal variation $\delta D(t)$ allows updating the initial value of the duty cycle control to reach the optimal total duty cycle $D^{opt}(t)$, where $D^{opt}(t) = D^g_{stc} - \delta D(t)^{10}$. This last one must be converted, for real-time implementation, to a control signal using the pulse width modulation PWM generator. It is essential to underline the fact that the synthesis of the robust controller requires the prior design of a linear model, which can take into account all exogenous effects that can impact the synthesized model

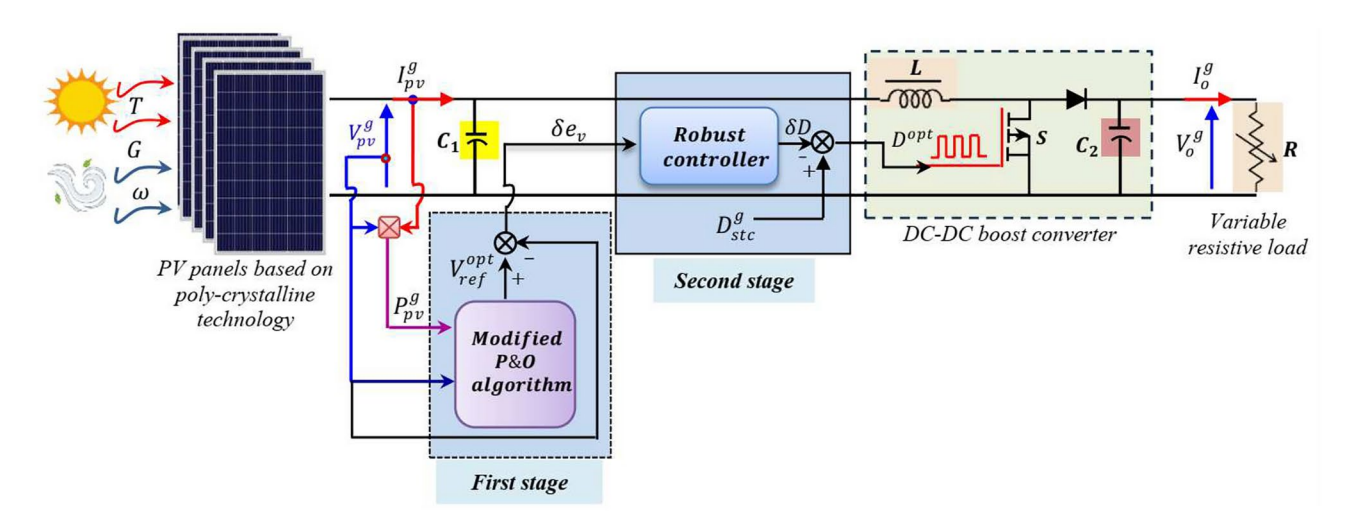


Figure 1. Control loop based on the proposed robust P&O-MPPT strategy.

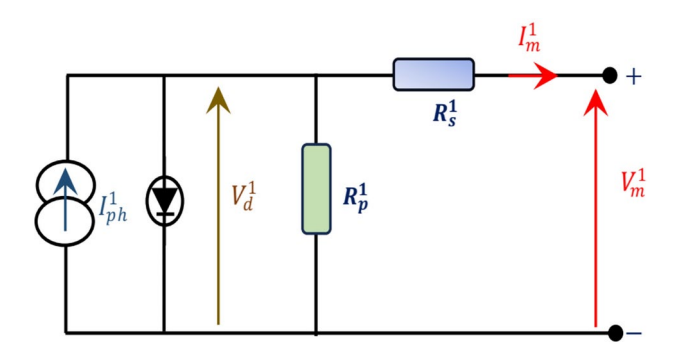


Figure 2. Equivalent electrical circuit of the overall solar PV cell.

in STC. In the present paper, the overall model of the SPCS is assumed to be uncertain due to the presence of another uncertain auxiliary model, describing the functioning of the PV array in STC. The corresponding equivalent electrical circuit has three key parameters, which must also be considered uncertain where its optimal tuning is ensured by the GA-based method.

Modeling of the PV panel

The desired model describing the functioning of a single PV panel based on poly-crystalline technology can be designed using the equivalent electrical circuit, as depicted in Fig. 2. This circuit is used to calculate the output current and voltage of both a single solar cell and the PV panel as a whole. It includes three key parameters to be optimized: the diode ideality factor n, the series resistance R_s^1 , and the shunt resistance $R_p^{10,18}$.

According to Fig. 2, the predicted current I_m^1 is given as a function of the model voltage V_m^1 using Eq. (1). It is given as below I_m^{12}

$$I_{m}^{1} = I_{ph}^{1} - I_{0d}^{1} \cdot \left(-1 + exp\left(\frac{V_{m}^{1} + R_{s}^{1} \cdot I_{m}^{1}}{n \cdot V_{T}^{1}}\right)\right) - \left(\frac{V_{m}^{1} + R_{s} \cdot I_{m}^{1}}{R_{s}^{1}}\right)$$
(1)

Moreover V_T^1 is the temperature voltage given by N_c number of series-connected PV cells per one PV panel, it is given by V_c^1

$$V_T^1 = \left(\frac{k \cdot T_c}{q}\right) \cdot N_c \tag{2}$$

Where $q=1.602176\times 10^{-19}~C$ is the electronic charge, $k=1.3806503\times 10^{-23}J/K$ is the constant of Boltzmann and n is the diode ideality factor. Also, T_c is a cell temperature depending on the three climatic conditions, such as the outdoor temperature T, the solar irradiance G and the wind speed ω . These parameters are related to the cell-temperature by the empirical relationship, given as below¹⁹

$$T_c = 1.14 \cdot (T - T_{stc}) + 0.0175 \cdot (G - 300) - K_r \cdot \omega + 30 \tag{3}$$

Here, K_r is a positive parameter given in manufacturer's data sheet. Moreover, the photo-current I_{ph}^1 corresponding one PV panel is defined by 15

$$I_{ph}^{1} = \left(\frac{G}{G_{stc}}\right) \cdot \left(I_{sh,0}^{1} + \alpha \cdot (T_{c} - T_{stc})\right) \tag{4}$$

From Eq. (4), the parameter α is a temperature coefficient corresponding to the STC value of the nominal short-circuit current $I^1_{sh,0}$ of one PV panel, Also, the reverse saturation current I^0_{ud} is expressed by 15

$$I_{0d}^{1} = I_{sr}^{1} \cdot \left(\frac{T_{c}}{T_{stc}}\right)^{\frac{3}{n}} \cdot \exp\left(\left(\frac{q \cdot E_{g}}{k \cdot n}\right) \cdot \left(\frac{1}{T_{stc}} - \frac{1}{T_{c}}\right)\right) \tag{5}$$

where, the band gap energy of the semiconductor $E_g=1.12\ V$ is measured across a diode and the corresponding diode current I^1_{sr} is given by I^5

$$I_{sr}^{1} = \frac{I_{sh,0}^{1} + \alpha \cdot (T_{c} - T_{stc})}{-1 + \exp\left(\frac{V_{oc}^{1} + \beta \cdot (T_{c} - T_{stc})}{n \cdot V_{T}^{1}}\right)}$$
(6)

Also, V_{oc}^1 is the open-circuit voltage, where β is the temperature coefficient corresponding to one PV panel based on poly-crystalline technology.

Parameter identification of the PV model

Let's consider x the design vector, regrouping the three preceding key parameters to be optimized, *i.e.*, $x = \left(n, R_s^1, R_p^1\right)^T$. The main goal is to find an optimal solution x^* within 3-dimensional search-pace, including the upper-bound vector $x_{\max} = \left(n_{\max}, R_{s_{\max}}^1, R_{p_{\max}}^1\right)^T$ and lower bound vector $x_{\min} = \left(n_{\min}, R_{s_{\min}}^1, R_{p_{\min}}^1\right)^T$, where each one must be previously chosen by the user²⁰. The desired optimal solution must be minimized, as much as possible, a fitness function, formulated as a quadratic sum of current discrepancies, generated when comparing the measured current $I_{pv}^1(k)$ with the predicted current $I_m^1(k)^{21}$, where this last one can be determined through the analytically solution of Eq. (1) using the *LambertW* function, available in MATLAB ® software²¹. The main idea is to set $V_{pv}^1 = V_m^1$ and then to formulate Eq. (1) in a general form, given by

$$Z = W(X)e^{W(X)} \tag{7}$$

In this case, Z is the argument of the real function W, whose exponential function $e^{W(X)}$ includes the real vector X. This vector thus presents the solution of Eq. (1), which is given in a general form, defined by

$$X = lambertW(Z) \tag{8}$$

From mathematical developments carried on Eq. (1) in accordance with the last general, we can obtain²¹

$$X = \left(\frac{R_s^1 \cdot R_p^1}{n \cdot V_T^1 \cdot (R_p^1 + R_s^1)}\right) \cdot I_{0d}^1 \cdot exp\left(\frac{V_m^1 + R_s^1 \cdot I_m^1}{n \cdot V_T^1}\right)$$
(9)

$$Z = \left(\frac{R_s^1 \cdot R_p^1}{n \cdot V_T^1 \cdot (R_p^1 + R_s^1)}\right) \cdot I_{0d}^1 \cdot exp\left(\frac{R_s^1 \cdot R_p^1 \cdot \left(I_{ph}^g + I_{0d}^g + \frac{V_m^1}{R_s^1}\right)}{n \cdot V_T^1 \cdot (R_p^1 + R_s^1)}\right)$$
(10)

Then, from Eqs. (9) and (10), the predicted PV current I_m^1 is given by²¹

$$I_{m}^{1} = \left(\frac{R_{p}^{1} \cdot \left(I_{ph}^{1} + I_{0d}^{1}\right) - V_{m}^{1}}{R_{p}^{1} + R_{s}^{1}}\right) - \left(\frac{n \cdot V_{T}^{1}}{R_{s}^{1}}\right) \cdot LambertW(Z)$$
(11)

Finally, the design problem of the PV model is formulated as a constrained optimization problem, whose fitness function $J(n,R_s^1,R_p^1)$ presents the mean square error MSE. It is stated below²¹

$$\begin{cases}
Min \\
n_{\min} \leq n \leq n_{\max} \\
R_{s_{\min}}^{1} \leq R_{s}^{1} \leq R_{s_{\max}}^{1} \\
R_{p_{\min}}^{1} \leq R_{p}^{1} \leq R_{p_{\max}}^{1}
\end{cases}
J = \frac{1}{m} \cdot \sum_{k=1}^{m} \left\{ I_{m}^{1} \left(k, n, R_{s}^{1}, R_{p}^{1} \right) - I_{pv}^{1}(k) \right\}^{2}$$
(12)

where m is the number of samples collected within the experimental test. Finally, the optimal solution of the preceding problem leads to the design of the desired overall PV model, in which the total series resistance R_s^g and the total shunt resistance R_p^g are respectively given by $R_s^g = \left(\frac{N_s}{N_p}\right) \cdot R_s^1$ and $R_p^g = \left(\frac{N_s}{N_p}\right) \cdot R_p^1$. Also, the total diode voltage V_d^g , where $V_d^g = N_s \cdot V_d^1$ is accordingly given by $V_d^g = V_m^g + R_s^g \cdot I_m^g$.

The linearization of the I-V characteristic resulting from the overall PV model

The linearization of the I-V characteristic, corresponding to the overall PV model for MPP, is a crucial step in finding the linear relationship between the total current I_m^g and total voltage V_m^g . This requires knowing the expression of the tangent line that must be drawn on the previous I-V characteristic at the point (V_{stc}^g, I_{stc}^g) , where total electrical power reaches its maximal (see Fig. 3). This leads to obtain 10,12

$$I_{m}^{g} = \left(\frac{\partial I_{m}^{g}\left(V_{stc}^{g}\right)}{\partial V_{m}^{g}}\right) \cdot V_{m}^{g} + \left(I_{m}^{g}\left(V_{stc}^{g}\right) - \left(\frac{\partial I_{m}^{g}\left(V_{stc}^{g}\right)}{\partial V_{m}^{g}}\right) \cdot V_{stc}^{g}\right)$$
(13)

The corresponding inverse slope leads to obtain the total equivalent resistor \widetilde{R}_{eq}^g , which is related with the total equivalent voltage source E_{eq}^g by the linear relationship, given as below 10,12

$$I_m^g = -\left(\frac{1}{\widetilde{R}_{eq}^g}\right) \cdot V_m^g + \left(\frac{1}{\widetilde{R}_{eq}^g}\right) \cdot E_{eq}^g \tag{14}$$

From Eqs. (13) and 14, the two electrical components \widetilde{R}_{eq}^g and E_{eq}^g are expressed by 10,12

$$\widetilde{R}_{eq}^g = \frac{1}{\left(\frac{1}{n \cdot V_{T_{stc}}^g} \cdot I_{0d}^g \cdot \exp\left(\frac{V_{stc}^g + R_s^g \cdot I_{stc}^g}{n \cdot V_{T_{stc}}^g}\right)\right) + \frac{1}{R_p^g}}$$

$$\tag{15}$$

$$E_{eq}^g = \widetilde{R}_{eq}^g \cdot I_{stc}^g + V_{stc}^g \tag{16}$$

 V^g_{stc} and I^g_{stc} are the STC values of V^g_m and I^g_m respectively. Correspondingly, the total reverse saturation current I^g_{0d} is given by $I^g_{0d} = N_p \cdot I^1_{0d}$. Also, the STC value of the temperature voltage V^g_{Tstc} is given by $V^g_{Tstc} = N_s \cdot \left(\frac{k \cdot T_c \cdot N_c}{q}\right)$. Typically, there is no unique solution to the above-constrained optimization problem.

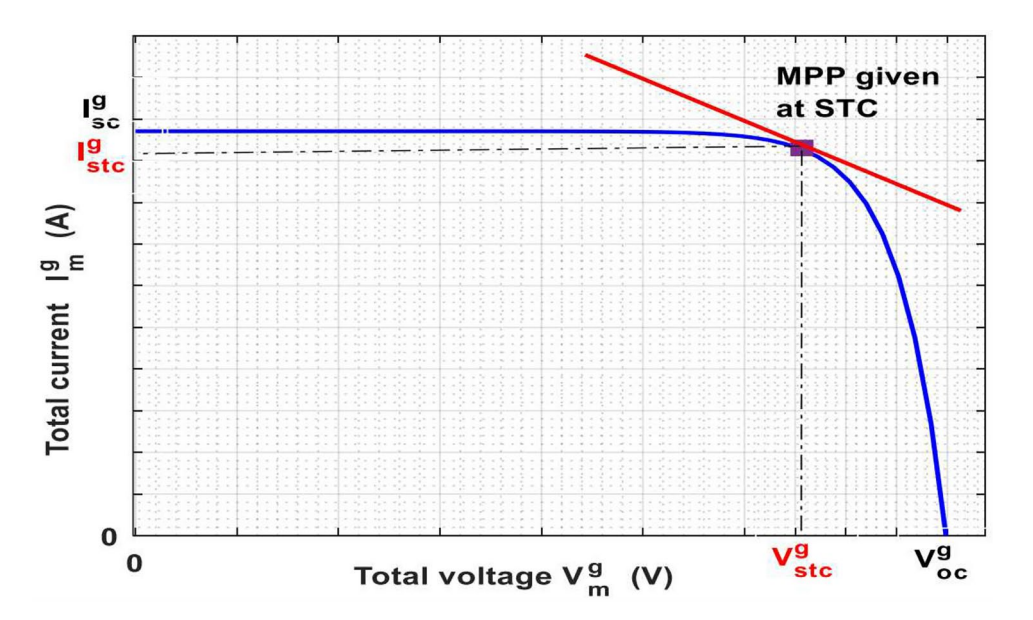


Figure 3. Linearization of the I-V characteristic around the STC.

This is due to the random behavior of the GA, whose exact solution depends on an appropriate choice of the two upper and lower limit vectors mentioned above. When the choice of these two limit vectors is too strict, the GA can remain stuck on one or more edges limiting the search space, so that the resulting solution satisfies certain constraints but does not explore more promising regions for the minimization of the fitness function. To overcome this problem, it is crucial to carefully extend the limit where the constraint is saturated. As a result, the previous linearization generates more than one tangent line in STC, leading to further doubts about the value of the equivalent resistance. As this value will play a decisive role in determining the overall model describing the actual functioning of the SPCS at STC, it must therefore be considered as an uncertain parameter, belonging within the range $\widetilde{R}_{eq}^g \in \left[\underline{R}_{eq}^g, \ \overline{R}_{eq}^g\right]$, where the upper limit \overline{R}_{eq}^g is given by $\overline{R}_{eq}^g = R_{eq}^g \cdot \left(1 + \Delta R_{eq}^g\right)$, while the lower bound \underline{R}_{eq}^g is given by $\underline{R}_{eq}^g = R_{eq}^g \cdot \left(1 - \Delta R_{eq}^g\right)$. In this concept, R_{eq}^g is the best value guaranteeing the deepest descent of the fitness function. It is therefore considered as the nominal equivalent resistance, where all other possible values of \widetilde{R}_{eq}^g are considered as uncertain resistances. Each one of them deviates from the nominal

value by a relative distance, given by $0 \le \left| \left(\widetilde{R}_{eq}^g - R_{eq}^g \right) / R_{eq}^g \right| \le 1$. Accordingly, it is possible to determine several neighboring models based on all possible values of \widetilde{R}_{eq}^g , where a perturbed model can describe one of the existing functioning of the actual SPCS behavior.

Modeling of the overall SPCS

The overall nonlinear model describing the functioning of the SPCS is determined using the electrical circuit shown in Fig. 4.

Accordingly, the corresponding nonlinear state-space representation is given by 9,10,12

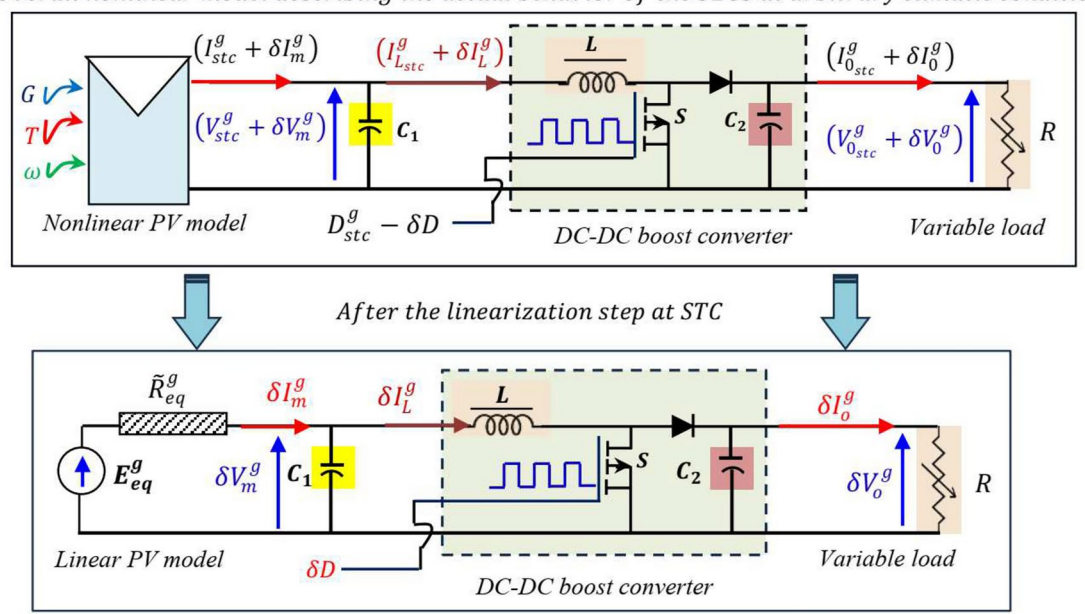
$$\frac{d}{dt}V_m^g(t) = \frac{1}{C_1} \cdot I_m^g(t) - \frac{1}{C_1} \cdot I_L^g(t)$$

$$\frac{d}{dt}I_L^g(t) = \frac{1}{L} \cdot V_m^g(t) - \left(\frac{1 - D(t)}{L}\right) \cdot V_0^g(t)$$

$$\frac{d}{dt}V_0^g(t) = \left(\frac{1 - D(t)}{C_2}\right) \cdot I_L^g(t) - \frac{1}{\widetilde{R} \cdot C_2} \cdot V_0^g(t)$$
(17)

where, I_L^g is the current traversing the inductance L where C_1 and C_2 are, respectively, the PV-side capacitor and load-side capacitor. Moreover, I_0^g and V_0^g are, respectively, the total current and total voltage, measured cross the variable resistive load R. Here, the STC value of the total voltage V_0^g is defined by $V_{0stc}^g = \sqrt{P_{stc}^g \cdot R}$, where

Overall nonlinear model describing the actual behavior of the SECS at arbitrary climatic conditions



Overall linear small – signal model describing the actual behavior of the SECS at STC

Figure 4. Linearization of actual SPCS behavior at STC.

 P_{\max}^g is the STC value of the total power, given by $P_{\max}^g = V_{stc}^g \cdot I_{stc}^g$. Also, the corresponding STC value of the total duty cycle control is given by $D_{stc}^g = 1 - \frac{V_{stc}^g}{V_{stc}^g}$.

To illustrate the small signal principle, we now consider the particular case of two state variables X(t) and Y(t). Each variable contains an STC value plus a small variation where, $X(t) = X_{stc} + \delta X(t)$ and $Y(t) = Y_{stc} + \delta Y(t)$. Also, let's consider the state variable Z(t), where $Z(t) = X(t) \cdot Y(t)$, which can also be given by the general form $Z(t) = Z_{stc} + \delta Z(t)$, where $Z(t) = (X_{stc} \cdot \delta Y(t) + Y_{stc} \cdot \delta X(t)) + X_{stc} \cdot Y_{stc} + \delta X(t) \cdot \delta Y(t)$. According to the small signal principle, it is obvious that all stationary quantities must be eliminated, and variations of order greater than or equal to 2 must also be removed. This leads to obtain the small state variation $\delta Z(t)$ where $\delta Z(t) = X_{stc} \cdot \delta Y(t) + Y_{stc} \cdot \delta X(t)$. In this case, the non-linearity around the STC of the state variable Z(t) now becomes linear, but around the equilibrium point. Applying now the same idea on the preceding nonlinear state-space representation using the following variable states Σ^{2} :

$$V_{m}^{g}(t) = V_{stc}^{g} + \delta V_{m}^{g}(t)$$

$$I_{m}^{g}(t) = I_{stc}^{g} + \delta I_{m}^{g}(t)$$

$$I_{L}(t) = I_{L}^{g} + \delta I_{L}^{g}(t)$$

$$V_{0}^{g}(t) = V_{0}^{gtc} + \delta V_{0}^{g}(t)$$

$$D(t) = D_{stc}^{g} - \delta D(t)$$
(18)

By replacing Eq. (18) in Eq. (17), we get²²

$$\frac{d}{dt} \left(V_{stc}^g + \delta V_m^g(t) \right) = \frac{1}{C_1} \cdot \left(I_{stc}^g + \delta I_m^g(t) \right) - \frac{1}{C_1} \cdot \left(I_{L_{stc}}^g + \delta I_L^g(t) \right) \\
\frac{d}{dt} \left(I_{L_{stc}}^g + \delta I_L^g(t) \right) = \frac{1}{L} \cdot \left(V_{stc}^g + \delta V_m^g(t) \right) - \left(\frac{1 - \left(D_{stc}^g - \delta D(t) \right)}{L} \right) \cdot \left(V_{0_{stc}}^g + \delta V_0^g(t) \right) \\
\frac{d}{dt} \left(V_{0_{stc}}^g + \delta V_0^g(t) \right) = \left(\frac{1 - \left(D_{stc}^g - \delta D(t) \right)}{C_2} \right) \cdot \left(I_{L_{stc}}^g + \delta I_L^g(t) \right) - \frac{1}{R \cdot C_2} \cdot \left(V_{0_{stc}}^g + \delta V_0^g(t) \right) \\$$
(19)

Similarly, by applying the small signal principle on Eq. (19), we get²²

$$\frac{d}{dt}\delta V_m^g(t) = \frac{1}{C_1} \cdot \delta I_m^g(t) - \frac{1}{C_1} \cdot \delta I_L^g(t)$$

$$\frac{d}{dt}\delta I_L^g(t) = \frac{1}{L} \cdot \delta V_m^g(t) - \left(\frac{1 - D_{stc}^g}{L}\right) \cdot \delta V_0^g(t) - \left(\frac{V_{0_{stc}}^g}{L}\right) \cdot \delta D(t)$$

$$\frac{d}{dt}\delta V_0^g(t) = \left(\frac{1 - D_{stc}^g}{C_2}\right) \cdot \delta I_L^g(t) - \frac{1}{R \cdot C_2} \cdot \delta V_0^g(t) + \left(\frac{I_{L_{stc}}^g}{C_2}\right) \cdot \delta D(t)$$
(20)

By applying the same preceding idea on Eq. (14), we get

$$\delta I_m^g(t) = -\frac{1}{\widetilde{R}_{eg}^g} \cdot \delta V_m^g \tag{21}$$

Finally, the uncertain linear small signal model, which links the model output $\delta V_m^g(t)$ with the model input $\delta D(t)$, is obtained by replacing Eq. (21) in Eq. (20). Consequently, the general form of its linear state-space representation is given by

$$\dot{x}_m(t) = \widetilde{A}_m \cdot x_m(t) + B_m \cdot \delta D(t)$$

$$\delta V_m^g(t) = C_m \cdot x_m(t)$$
(22)

where $x_m(t)$ is the state vector regrouping the three state variables δV_m^g , I_L^g and δV_0^g , i.e., $x_m(t) = (\delta V_m^g, \delta I_L^g, \delta V_0^g)^T$. Moreover, the input matrix B_m and the output matrix C_m are defined by

 $B_m = \left(0, -\frac{V_{0stc}^g}{L}, \frac{I_{Lstc}^g}{C_2}\right)^T$ and $C_m = (1,0,0)$ respectively. Also, the uncertain state matrix \widetilde{A}_m is defined by Eq.23, given as below

$$\widetilde{A}_{m} = \begin{pmatrix} -\frac{1}{C_{1} \cdot \widetilde{R}_{eq}^{g}} & -\frac{1}{C_{1}} & 0\\ \frac{1}{L} & 0 & -\left(\frac{1 - D_{stc}^{g}}{L}\right)\\ 0 & \frac{1 - D_{stc}^{g}}{C_{2}} & -\frac{1}{R \cdot C_{2}} \end{pmatrix}$$
(23)

Assuming there is no uncertainty regarding the equivalent resistance in the overall PV model, i.e., $\Delta R_{eq}^g=0$, it is possible to determine the nominal transfer function $G_n(s)$ based on the uncertainty-free part matrix

 A_m using the following relationship $G_n(s) = C_m \cdot (s \cdot I_{3 \times 3} - A_m)^{-1} \cdot B_m$, where s is the Laplace operator, $I_{3 \times 3}$ is the identity matrix having the same size as matrix A_m . Accordingly, the perturbed transfer function $G_P(s)$ is expressed concerning the nominal one using the relationship $G_p(s) = G_n(s) \cdot (1 + \Delta_m(s))$, where the unknown transfer function $\Delta_m(s)$ must be satisfied the robustness condition $|\Delta_m(s)| \leq 1$. It includes all relative distances, that occurred between the nominal model $G_n(s)$ and all possible perturbed models $G_p(s)$. In this paper, these distances are assumed to be unstructured multiplicative uncertainties.

Design of the robust fixed-order H_{∞} controller

Consider the closed-loop system including the robust controller K(s). This last one is connected in series with the perturbed model $G_p(s)$ (see Fig. 5a). Similarly, consider the uncertain parameter \widetilde{R}_{eq}^g , which appeared in the state matrix \widetilde{A}_m of the previous overall model. The inter-model distances generated between the nominal model $G_n(s)$ and any neighboring uncertain model $G_p(s)$ are considered as unknown relative uncertainties. It is modeled by the unstructured multiplicative uncertainty $\Delta_m(s)$, which is expressed by $2^{3,24}$

$$\Delta_m(s) = G_n^{-1}(s) \cdot (G_p(s) - G_n(s)) \tag{24}$$

According to the robust control design methodology, the first step is to separate all modeling uncertainties from the nominal model $G_n(s)$. This allows for establishing the closed-loop system, illustrated in Fig. 5b. Based on the worst-uncertainty case occurring in the perturbed model $G_p(s)$, the curves of maximal singular values of all preceding uncertainties $\sigma_{\max}\left[\Delta_m\left(\omega_m\right)\right]$ must be majorized, over the frequency rang $\omega_m\epsilon\left(\omega_{m_{\min}},\ \omega_{m_{\max}}\right)$, by the curve of the ones corresponding $\sigma_{\max}\left[W_y\left(\omega_m\right)\right]$. This leads to satisfy the inequality relationship, given by Eq. (25) as below^{23,24}

$$\sigma_{\max}\left[W_y\left(\omega_m\right)\right] > \sigma_{\max}\left[\Delta_m\left(\omega_m\right)\right]$$
 (25)

In this paper, the transfer function $W_y(s)$ is determined by the MATLAB function *ucover*. MATLAB It is then used to penalize the model output δV_m^g for providing the exogenous output z_y (see Fig. 5c). The main aim is to minimize, as much as possible, the energy of the weighting function output z_y , regardless of any change in the exogenous input δV_{ref}^g . This requires satisfying the RS condition, formulated as below^{23,24}

$$RS: \|W_y(s) \cdot T_y(s)\|_{\infty} \le 1 \iff \|T_y(s)\|_{\infty} \le \frac{1}{\|W_y(s)\|_{\infty}}$$

$$(26)$$

where, $\|X(s)\|_{\infty}$ is an H_{∞} -norm of the transfer function X(s), which defines the largest threshold in the curve of $\sigma_{\max}[X(\omega_m)]$ over the frequency rang $\omega_m \epsilon(\omega_{m_{\min}}, \ \omega_{m_{\max}})$. Also, the transfer function $T_y(s)$, where $T_y = G_n K \cdot (I + G_n K)^{-1}$ is the complementary sensitivity that associates the total set point voltage δV_{ref}^g

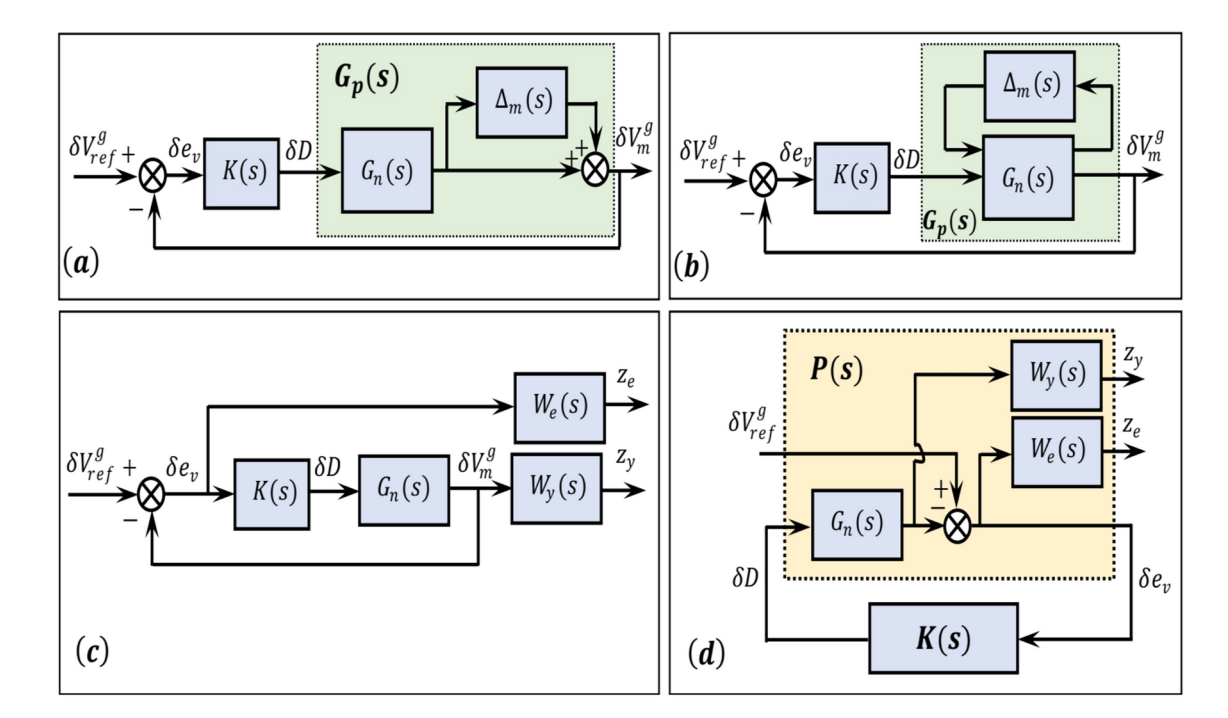


Figure 5. Different block diagrams used for the synthesis of the robust fixed-order H_{∞} controller.

with the total output voltage δV_m^g . According to the robust control design methodology, another complementary condition on NP must also be verified in conjunction with the previous RS condition. It is given by 24,25

$$||W_e(s) \cdot S_y(s)||_{\infty} \le 1 \tag{27}$$

where $W_e(s)$ is a stable transfer function, selected previously by user. Its general form is expressed as below 26,27

$$W_e(s) = \frac{\frac{s}{M_s} + \omega_B}{s + \omega_B \cdot \xi_s} \tag{28}$$

the perfect form to be established for the direct sensitivity function $S_y(s)$ Also, ξ_s is the desired steady-state tracking error. It is essential to point out that the weighting function $W_e(s)$ is used to penalize the voltage error δe_v for providing the exogenous output z_e (see Fig. 5c). Here, the main aim is to minimize, as much as possible, the weighting function output z_e , regardless of any change in the exogenous input δV_{ref}^g . Moreover, the transfer function $S_y(s)$, where $S_y = (I + G_n K)^{-1}$ is the direct sensitivity that associates the error voltage δe_v with the total output voltage δV_m^g .

Because of the identity $T_y + S_y = 1$, satisfying these two conflicting objectives in the same frequency point poses a major challenge for most designers^{5,6}. This in turn leads to finding a specific robust controller among existing ones, able to achieve a good NP/RS trade-off. These two conditions must therefore be combined into a single one, to provide the "weighted-mixed sensitivity problem". The problem can be formulated using the standard formalism shown in Fig. 5d²⁶. Accordingly, P(s) is the generalized synthesized model including the nominal model and the two preceding weighting functions. The main goal is to minimize, as much as possible, the H_{∞} -norm of resulting linear fractional transformation LFT, given by the interconnection system between both P(s) and K(s). This leads to satisfy the NP/RS trade-off condition, expressed by^{27,28}

$$RS/NP: \left\| \begin{array}{c} W_y(s) \cdot T_y(s) \\ W_e(s) \cdot S_y(s) \end{array} \right\|_{\infty} \le \gamma < 1 \tag{29}$$

where the parameter γ is the H_{∞} performance level to be reached. The problem, given by Eq. (29), is solved by the MATLAB function *hinfstruct*, whose controller-order to be synthesized must prior be specified by the user through preselecting the dimension of the evolution matrix providing the state representation of desired controller. Afterward, the two transfer functions for the two weighting functions $W_e(s)$ and $W_y(s)$ are introduced and the transfer function of the nominal model is then computed from the linear state-space representation of the overall small-signal model.

Now, the three preceding transfer functions are used to compute the generalized model P(s) by which the weighted-mixed sensitivity criterion is formulated. Its solution resulting the state-space representation of desired robust controller. All the above steps must be repeated as the H_{∞} performance level γ is greater than unity, i.e., $\gamma > 1$. In this case, other parameters must be chosen for the weighting function $W_e(s)$, and the preceding steps are again repeated until obtaining $\gamma < 1$. Once the solution is accepted, the two direct and complementary sensitivity functions are computed and the two robustness conditions RS and NP are verified in the frequency domain.

Performance assessments of the proposed robust P&O-MPPT strategy Experimental test description

TThe experimental test was carried out using a set of PV panels placed on the roof of the faculty, located at Yildiz University, in Istanbul, Turkey²⁹. There are three types of PV panels, some of them are based on thinfilm technology, others are based on poly-crystalline technology and the remaining ones are based on monocrystalline technology. In this paper, only the second PV panel type is considered. Consequently, the SPCS to be modeled and then controlled consists of three distinct devices, such as the PV array, the DC-DC boost converter, and the variable resistive load. Moreover, the PV array includes four PV panels. Each one is connected in series with the other PV panels. The modeling step of the resulting PV array is performed using the equivalent electrical circuit, whose set of three key parameters is optimized by the GA. The real-time measurements of the actual total current were previously recorded as a function of three real-time measurements of the outdoor temperature, solar irradiation, and wind speed of the environment. Next, the performances of the proposed robust P&O-MPPT strategy are evaluated and compared, at the STC, with those provided by the improved P&O-MPPT strategy, which includes in its second stage either the parallel PID controller or the ideal PID controller. Finally, the validity of this strategy is verified on a day chosen from the remaining set of real-time measurements. These three sets of samples were recorded as part of the experimental test available at the aforementioned faculty, in which the existing measurements were collected hourly over one month, starting at 9 a.m. on September 9th, 2023. A total of 702 samples of total currents and total voltage were collected as a function of the same number of samples, collected for solar irradiance using a Kipp-Zonen CMP21 pyranometer²⁹, where this last one was previously placed at an inclination angle of 41° on the roof of this faculty. Similarly, the same number of samples were recorded for outdoor temperature using a thermocouple sensor based on the Campbell CS215 instrument²⁹. Finally, the same number of samples was also recorded for wind speed using a specific tachymeter. Figure 6



Figure 6. PV panels and measuring devices used in the experimental test.

	$I_{PV}^g(A)$	$V_{PV}^g(V)$	$G(Wm^{-2}]$	T (°C)	$\omega(m\ s^{-1}]$
Minimal value	0	1.1383	0	13.600	0.2133
Maximal value	8.3811	130.19	759.47	32.712	26.658

Table 1. Minimal and maximal limits recorded for all real-time measurements during 1 month.

therefore shows the image presenting this experimental test, including the various measuring instruments required to carry out these real-time measurements²⁹.

Among all previous real-time measurements, the minimal and maximal values corresponding to each real-time measurement are summarized in Table 1 given as below measuring devices used in the experimental test

Starting from the upper and lower limits summarized in Table 1, it is clear that STC conditions are not reached throughout the above-mentioned period. Since the assessment of the performance of any control strategy must be carried out in STC, the goal is to design the equivalent electrical circuit that can guarantee the most accurate prediction of the overall model in STC. For this purpose, the previous 702 samples are divided into 300 samples used to identify the PV model, 200 samples used to validate this model, and finally part of the 202 remaining samples are used to verify the performance of the proposed robust P&O-MPPT strategy.

Computing the parameters of the overall model describing the PV array

This aim is achieved through an initial design of the model corresponding to one PV panel based on polycrystalline technology. The GA is applied to optimally find the three key parameters of the corresponding equivalent electrical circuit using the first set of 300 samples. The GA tuning parameters required for this step can be summarized in Table 2, presented as below

Also, the data-sheet corresponding one PV panel can be summarized in Table 3, given as below

Then, the search space corresponding to the constrained optimization problem is chosen after several runs of the GA, during which several extensions are performed where the solution is stuck in one or more of the saturated constraints. The most appropriate, but not exclusive, choice that avoids any eventual saturation is the one given as follows:

$$0.8 \le n \le 1.5
0.01 \le R_s^1 \le 1
670 \le R_p^1 \le 800$$
(30)

As a result, the best minimization of the fitness function is the one given by $J_{\min}=0.4226$, providing the following nominal parameters n=1.301, $R_s^1=0.105~\Omega$ and $R_p^1=795.771~\Omega$, where the nominal total series resistance and nominal total shunt resistance are accordingly given by $R_s^g=0.42\Omega$ and $R_p^g=3183.08~\Omega$ respectively. Therefore, Fig. 7 depicts the overall model describing the actual PV array. On the left-hand side of the overall model, there are two manual switches enabling the selection of PV array functioning at STC, providing the nominal MPP position in I-V characteristic. Also, Fig. 8 compares the model's total current with the measured total current using the second set of 200 real-time measurements

Parameters		Value		
Generation nur	nber	60		
TolFun		10^{-6}		
Population size		60		
PlotFcns		gaplotbestfun		
	Elite count	1.85		
Reproduction	Crossover	0.85		
Mutation funct	ion	Constraindependent		
Crossover function		Scattered		
	Direction	Forward		
Migration Fraction		0.22		

Table 2. GA setting parameters to solve the design model problem of the overall PV array.

Parameter		Value	Unit	
	P^1_{stc}	280	W	
	V_{stc}^1	32.29	V	
	Voc^1_{stc}	39.69	V	
	$Istc^1_{stc}$	8.68	A	
STC	Isc^1_{stc}	9.12	A	
α		0.05	%/°C	
β		0.32	%/°C	
K_r		1.468	-	

Table 3. Data sheep characterizing one PV panel based on monocrystalline technology.

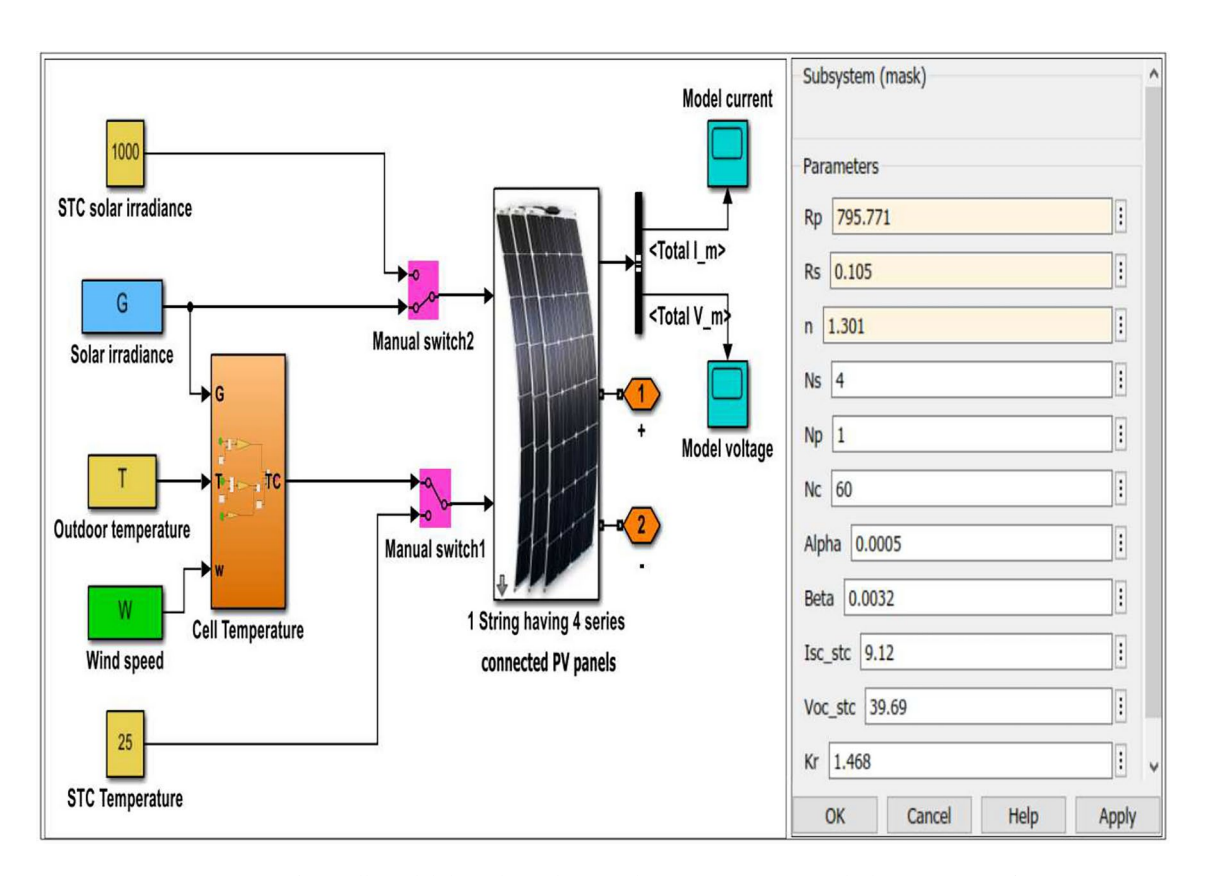


Figure 7. Design of overall model describing the actual PV array using Simulink MATLAB software.

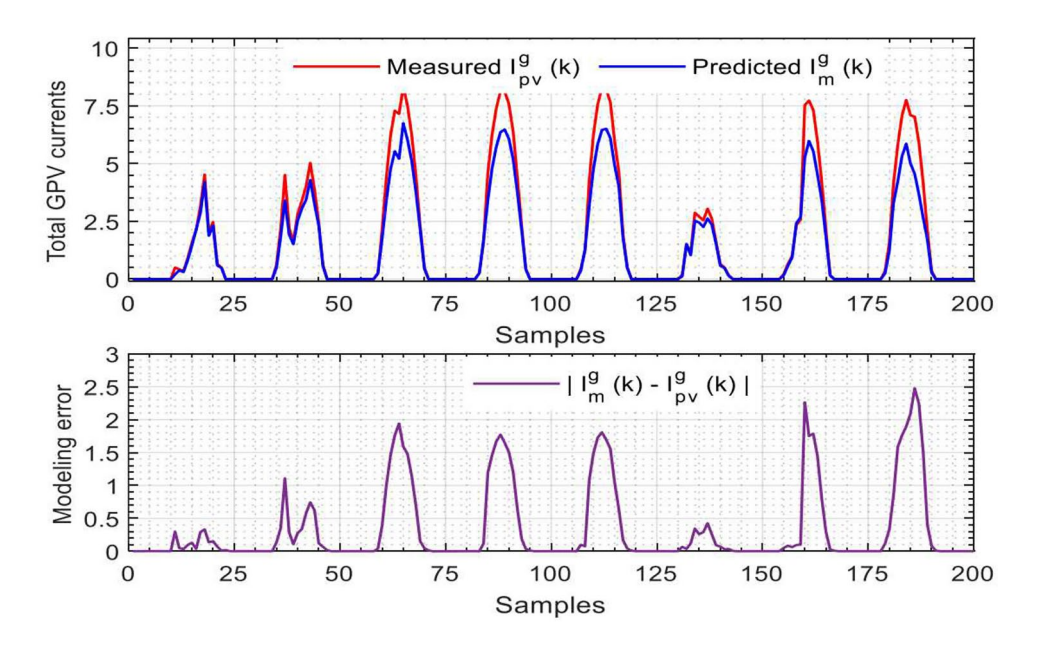


Figure 8. Validation of overall PV model using further real-time measurements.

Parameter	C_1	C_2	L	f_c	$I_{L_{stc}}^g$
Value	20.87	137.50	3.00	15.00	8.68
Unit	μH	μH	mН	KHz	A

Table 4. Parameters used to determine the overall linear uncertain model of the SPCS.

From Fig. 8, it is easy to confirm that the GA provides a good minimization of the fitness function, as the three resulting key parameters allow building up an acceptable PV model in terms of modeling accuracy. Furthermore, this model provides a good prediction of the actual total current despite employing additional samples that were not previously utilized in the parameter identification step and are considered as unknown measurements for this PV model. Now, thanks to Eqs. (15) and (16), the I-V linearization at STC which corresponds to the overall PV model provides the two nominal parameters $R_{eq}^g=22.155\Omega$ and $E_{eq}^g=321.47\ V$ where this last one is not considered in determining the overall model of the SPCS due to the application of the small signal principle on Eq. (19). Also, applying the GA with other initial generations results in providing other neighboring values of the three preceding nominal key-parameters, whose equivalent resistance values are offset from the nominal one by the upper limit $\overline{R}_{eq}^g=26.586\ \Omega$, and by the lower limit $\underline{R}_{eq}^g=17.724\ \Omega$, resulting therefore in a worst-case uncertainty of $\Delta R_{eq}^g=20\%$ concerning the nominal value.

Computing the parameters of the overall model describing the behavior of the SPCS

When the resistive load to be supplied is chosen by $R=100~\Omega$. According to Tab.3, the STC value of the total load-voltage V_0^g is given by $V_{0stc}^g=\sqrt{V_{stc}^g\cdot I_{stc}^g\cdot R}$, yielding also to obtain $V_{0stc}^g=334.83~V$. This leads also to obtain the STC value of the duty cycle $D_{stc}^g=0.61425$. Finally, the parameters used for SPCS control can be summarized in Table 4, given by

Consequently, when $\Delta R_{eq}^g=0$, the linear small-signal nominal model is derived from the uncertain linear state-space representation. It is given by

$$\dot{x}_m(t) = \begin{pmatrix} -2162.7 & -47916 & 0\\ 333.33 & 0 & -128.58\\ 0 & 2805.4 & -72.727 \end{pmatrix} \cdot x_m(t) + \begin{pmatrix} 0\\ -111610\\ 63127 \end{pmatrix} \cdot \delta D(t)$$
(31)

where the corresponding transfer function is given by

$$G_n(s) = \frac{53479 \times 10^5 \cdot (s + 145.5)}{(s + 119.6) \cdot (s^2 + 2116 \cdot s + 162.4 \times 10^5)}$$
(32)

So, it is a nominal model presenting the high static gain $G_n(0) = 400.6$, from which it is possible to synthesize the robust voltage controller using the PID structure, whose parameters are determined by applying the MATLAB function $PidTuner^{30}$. Accordingly, the graphical user interface GUI is opened, in which some frequency-domain

specifications must previously be selected for tuning the gains of the voltage PID controller. It depends on selecting both the desired bandwidth ω_B and the desired phase margin φ . Indeed, the first tuning parameter is chosen in a similar to the one used in synthesizing the robust fixed-order H_∞ controller, i.e., $\omega_B=120\ rad/s$, while the second tuning parameter is chosen according to the visualization of the resulting step response of the closed loop system, where the best one is given by $\varphi=63^\circ$. In the time-domain specifications, the two preceding tuning parameters lead to ensuring the response time $T_s=0.01667\ sec.$, and the robustness ratio of 63.6%. Finally, the resulting tuning parameters provide only the robust PI controller structure, whose transfer function is given by

$$K_0(s) = 2.73 \cdot 10^{-7} + \frac{0.32773}{s} \tag{33}$$

Computing the parameters of the robust fixed-order H_{∞} controller

Frequency-domain analysis

In the synthesis step of the robust fixed-order H_{∞} controller, the uncertain equivalent resistance R_{eq}^g must cover all possible values ranging from its lower limit $\underline{R}_{eq}^g = 17.724~\Omega$ up to its upper limit $\overline{R}_{eq}^g = 26.586~\Omega$, using the step size 0.01. This generates 21 perturbed models and therefore a total of 21 relative errors concerning the nominal model. The MATLAB function *ucover* is then run with the choice of the degree of the RS weighting function, thus providing the parameters for the primary weight $W_y(s)^{31}$. A perfect form can be achieved when the curve of $\sigma_{\max}\left[W_y\left(\omega_m\right)\right]$ does not exceed the 0_{dB} condition at low frequencies, in particular below a user-selected pulsation, called ω_{BT} , where $\omega_B\ll\omega_{BT}^{5,32}$. This last one authorizes the level at which the modeling errors can be committed during the modeling step of the SPCS behavior^{5,32}.

keeping with the previous restriction, the given $W_y(s)$ is multiplied by a gain of 10, to increase 10 times the primary safety margin corresponding to the above-mentioned RS weighting function (see Fig. 9). This leads to a obtain $\omega_{BT}=2477\ rad/s$ and the desired RS weighting function $W_y(s)$, which is given by

$$W_y(s) = \frac{0.47254 \cdot \left(s^2 + 10360 \cdot s + 4083 \times 10^4\right)}{s^2 + 2282 \cdot s + 2114 \times 10^4}$$
(34)

The next step used for the controller design requires determining the NP weighting specification where the corresponding transfer function is previously mentioned in Eq. (28). In the present paper, the parameters $M_s=1.25$, $\omega_B=120~rad/s$ and $\xi_s=10^{-3}$ are chosen to determine the transfer function of $W_e(s)$, which also rewritten as the following form

$$W_e(s) = \frac{0.8 \cdot (s + 150)}{s + 0.12} \tag{35}$$

According to Eqs. (34) and (35), the controller design problem is formulated as the weighted-mixed sensitivity function where its optimal solution is ensured by the preselected controller-order $d^o\left(K_H(s)\right)=3$ where the MATLAB function *hinfstruct* is run using 10 random initializations. The NP/RS trade-off condition is verified

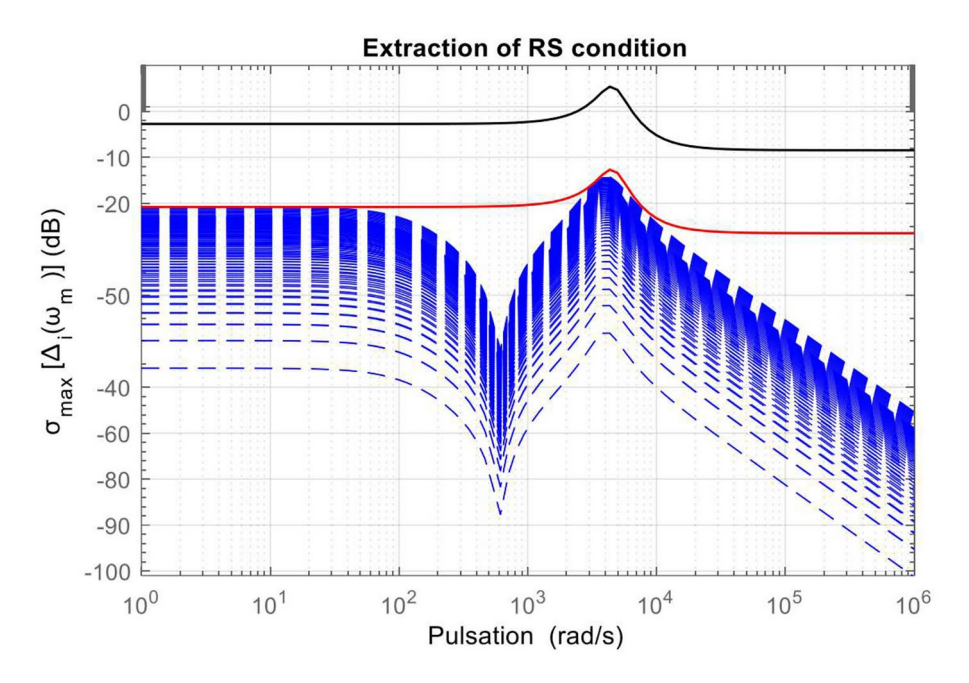


Figure 9. Presentation of all possible relative modeling errors used to extract the RS condition.

within the frequency range $\omega_m \epsilon \left(10^1 \quad 10^6\right) \ rad/s$ where the optimal criterion minimization is reached by providing the H_{∞} performance level $\gamma = 0.91191$. The resulting transfer function of the robust fixed-order H_{∞} controller is given by

$$K_H(s) = \frac{33.767 \times 10^{-5} \cdot \left(s^2 + 221.6 \cdot s + 16300\right)}{\left(s + 0.1683\right) \cdot \left(s + 104.7\right) \cdot \left(s + 202.1\right)}$$
(36)

The NP/RS trade-off condition is thus verified in the previous frequency range, leading to Fig. 10.

From Fig. 10, it can be seen that the plot of the maximal singular values of NP/RS condition for the robust P&O-MPPT strategy is below the boundary condition, i.e. 0 dB at all frequency points. On the other hand, the condition is violated at low frequencies for the standard P&O-MPPT strategy, which can be explained in the time domain by obtaining poor reference tracking properties, as well as by a large time required to attenuate exogenous effects caused by model uncertainties.

Time-domain analysis

To confirm all the previous findings, in the time domain, the closed loop systems based on the robust PI controller and the one based on the robust fixed-order H_{∞} controller are simultaneously excited by two distinct inputs. The first one consists of a unit step applied for 0.1 hours. The aim is to ensure a perfect tracking dynamic, characterized by a fast rise time, large stabilization time, acceptable overshoot, and zero steady-state error.

Additionally, the second input consists of a perturbation input, characterized by a bounded energy of 20% of the set point input amplitude. It is applied just at the starting time t=0.05~h, and it is carried on the nominal model output. The aim is to ensure a good robustness margin concerning the perturbation input, whose attenuation must be guaranteed within a short time range. Knowing that the two preceding dynamics characterize the two conflicting objectives, i.e., tracking/regulation, are examined not only for the nominal operating state of the SPCS where the corresponding output responses are mentioned using solid lines. Also, they are examined in the presence of 21 perturbed operating states where the corresponding output responses are outlined using dash lines. Therefore, Fig. 11 compares the NP/RS trade-offs of the two preceding strategies in the presence of 21 perturbed models.

According to Fig. 11, the better properties for the two performances and robustness are ensured by the proposed robust P&O-MPPT strategy even in the presence of unstructured multiplicative uncertainties. Now, the performance assessments are carried out at STC for the two preceding strategies using the closed loop system, established by sim-power systems of MATLAB software (see Fig. 12). The control loop, depicted in Fig. 12, has two manual switches enabling the commutation between the use of the real-time climatic conditions or the STC ones. Based on these commutators, the performances of the two preceding strategies can be compared in STC using the time range $t\epsilon[0,~0.14]~h$. Accordingly, the modified P&O algorithm, needed for the first stage of the two preceding strategies, is initialized by the STC values for the total current and voltage. Here, the fixed step size updating the nominal reference voltage is given by $\delta V = 10^{-3}$.

Therefore, Fig. 13 shows the comparison between the voltage error, minimized by the robust PI controller, and the one minimized by the proposed robust fixed-order H_{∞} controller. Also, Fig. 14 compares the reference tracking dynamic of the optimal reference voltage, generated by the modified P&O algorithm for the two preceding strategies. Figure 15 compares the generated power by the PV array and the consumed power by the

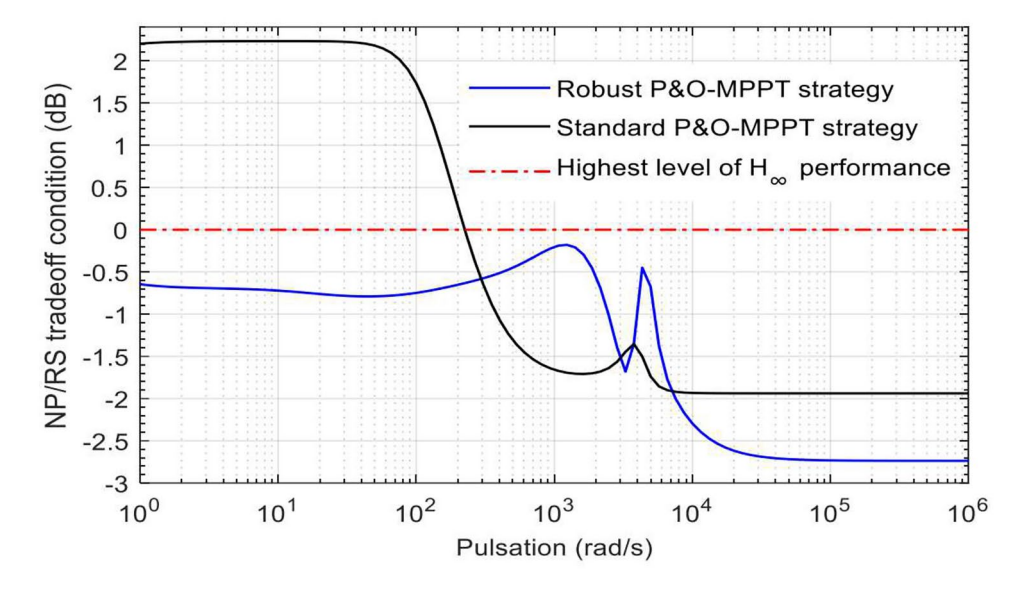


Figure 10. Verifying NP/RS trade-off condition by standard and robust P&O-MPPT strategies.

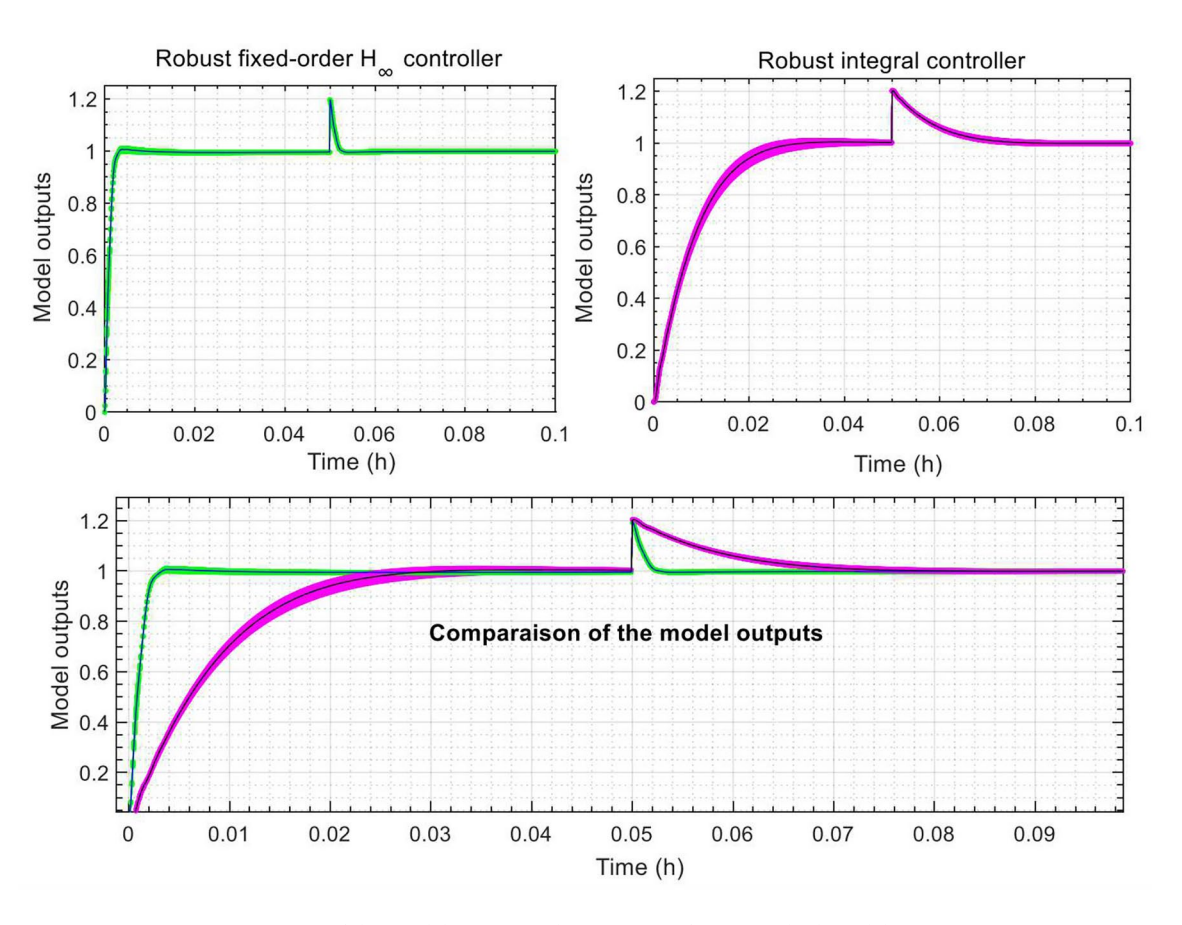


Figure 11. Comparison of the model output in the presence of 21 perturbed model uncertainties.

resistive load using the two preceding strategies and finally Fig. 16 compares the two corresponding duty cycle controls

From Fig. 14, it is easy to confirm that the modified P&O algorithm generates the optimal reference voltage closest to the one previously recorded at STC, i.e., $V_{ref}^{opt}=N_s\cdot V_{pv}^1=129.16~V$. This is properly tracked by the total voltage based on the proposed robust fixed-order H_{∞} controller at the starting time t=0.08~h. On the other hand, for the same previous setpoint, the reference tracking dynamic is achieved at the starting time t=0.11~h. This means that an improvement ratio of 37.5% can be guaranteed by the proposed strategy, which is therefore considered to outperform as compared to the standard one.

Consequently, the maximal power extraction ratio, ensured by the proposed strategy, is improved 400 times when compared to the SPCS that is controlled by the standard P&O-MPPT strategy (see Fig. 15). As already mentioned, the nominal value of the duty cycle is given by $D_{stc}^g = 0.61425$. Consequently, the proposed strategy achieves this value quickly within a stabilization time that starts at $t=0.04\ h$. In contrast, with the standard P&O-MPPT strategy, there is a 300-fold delay when comparing its settling time to the one provided by the roust P&O-MPPT strategy. This means that a massive loss of energy extraction can be observed when the SPCS is controlled by the standard P&O-MPPT strategy.

The closed-loop system based exclusively on the proposed strategy is finally run during the time t=12~h of a one-day period chosen arbitrarily from one preceding month. the corresponding samples among the 202 remaining samples found in the third set. In this case, the solar irradiance value is started from zero, passed through its high-point $\overline{G}=696.417~W\cdot m^{-2}$ and returned again to zero at the end of the same day. During the same period, the resistive load is set at $R=120\Omega$ for the first 7 hours, then reduced to $R=80\Omega$ for the remaining five hours. Similarly, the outdoor temperature value is initially recorded by $T=17.505^{\circ}C$, passed through its maximal value $T=22.745^{\circ}C$, then returned to the value $T=20.083^{\circ}C$ at the end of the same day. Finally, the wind speed value is counted from $\omega=4.533~m/s$ and then finished by $\omega=12.7617~m/s$. As a result, Fig. 17 clearly shows the climatic evolution of the three preceding climatic parameters during the same day. Also, Fig. 18 represents the power produced by the PV array and the power consumed by the variable resistive load. Finally, Fig. 19 shows the duty cycle control generated within 12 hours by the proposed robust fixed-order H_{∞} controller.

According to Fig. 18, the two powers generated and consumed have the same shape as the one of the measured solar irradiances. Here, the curve of the consumed power is subjected to a rapid change at time t=7s due to the sudden modification of the resistive load, which has suddenly decreased by a ratio of 40% with respect to the corresponding nominal value. Therefore, thanks to the robust fixed-order H_{∞} controller, the closed-loop

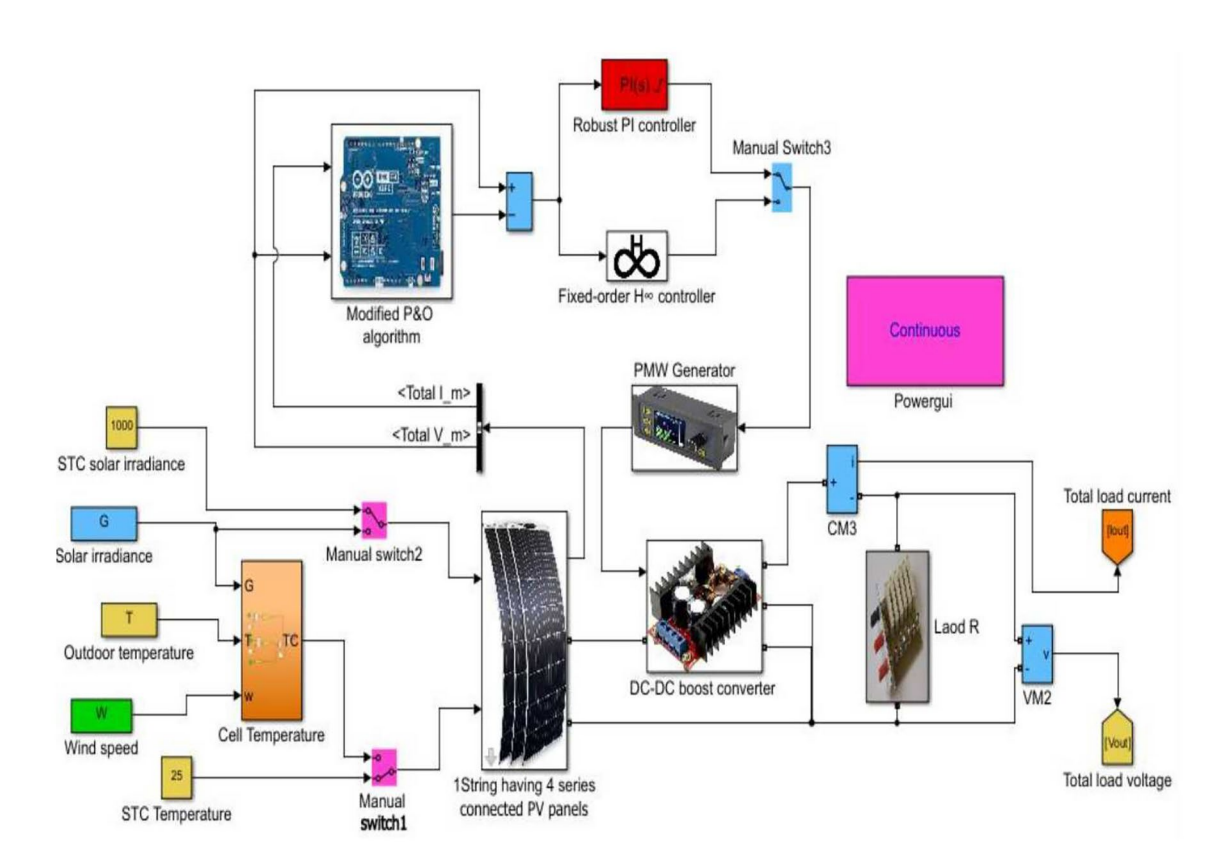


Figure 12. Performance assessments at STC for the two strategies using sim-power systems.

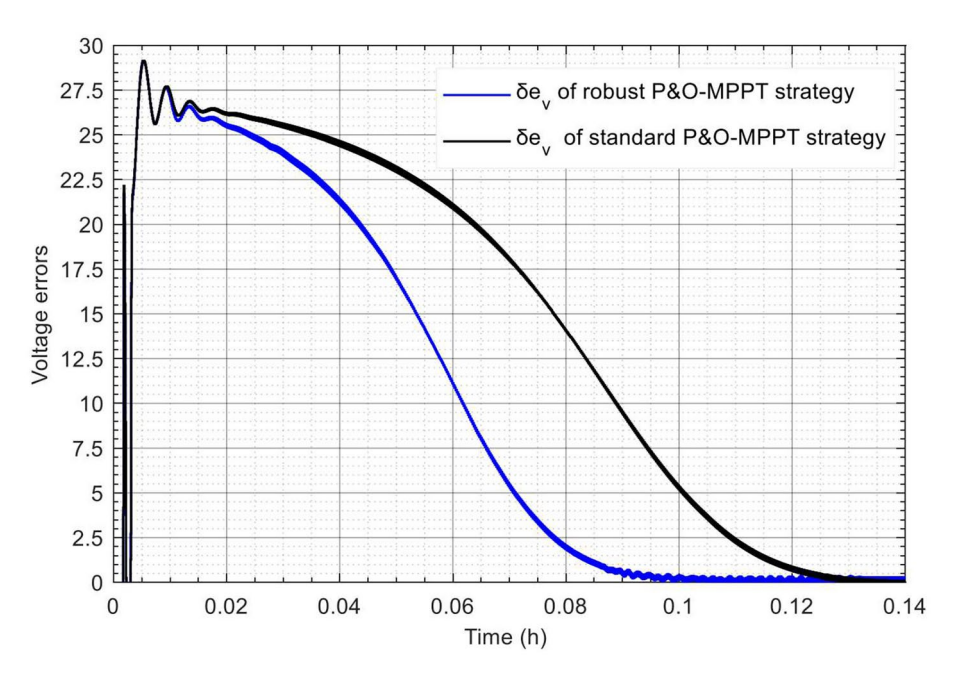


Figure 13. Comparison of the resulting voltage errors for standard and robust P&O-MPPT strategies.

system becomes insensitive to this external change, where the robust P&O-MPPT strategy correctly detects the sudden change coming from the measured total voltage, providing the required optimal reference voltage through its first phase using the modified P&O algorithm, The proposed controller, in turn, enables the duty cycle to increase from 0.55 to 0.455 as the load is reduced (see Fig. 19). Knowing that the nominal value of this resistive load is already introduced in the nominal model computation. Thanks to the 10-fold increase

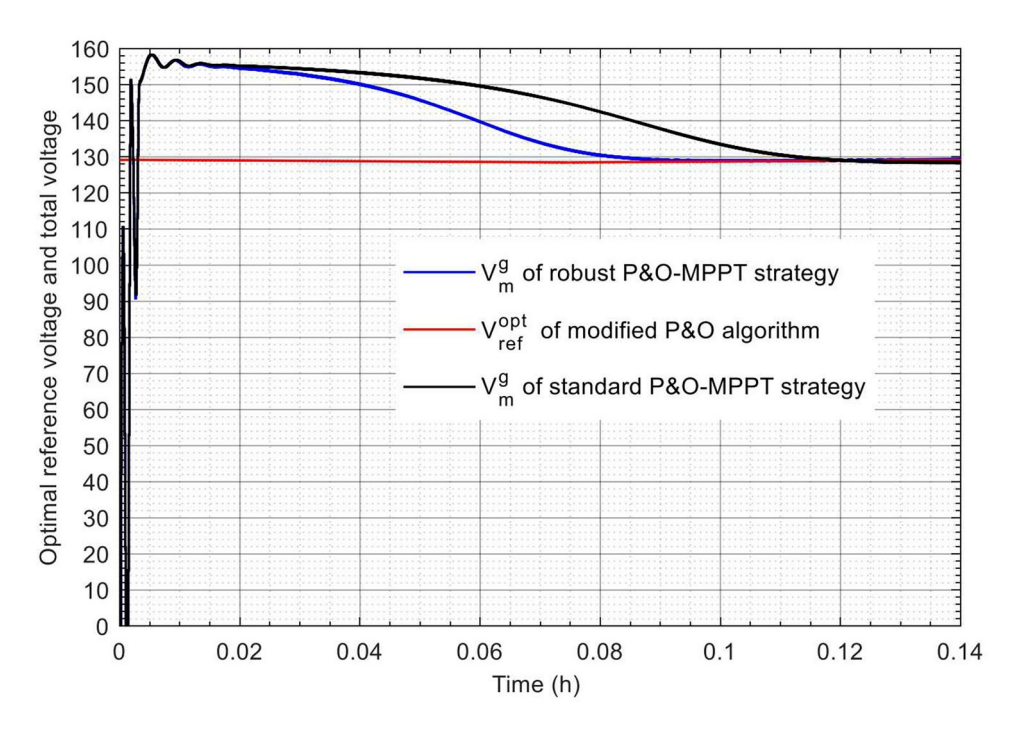


Figure 14. Comparison of the reference tracking dynamics for standard and robust P&O-MPPT strategies.

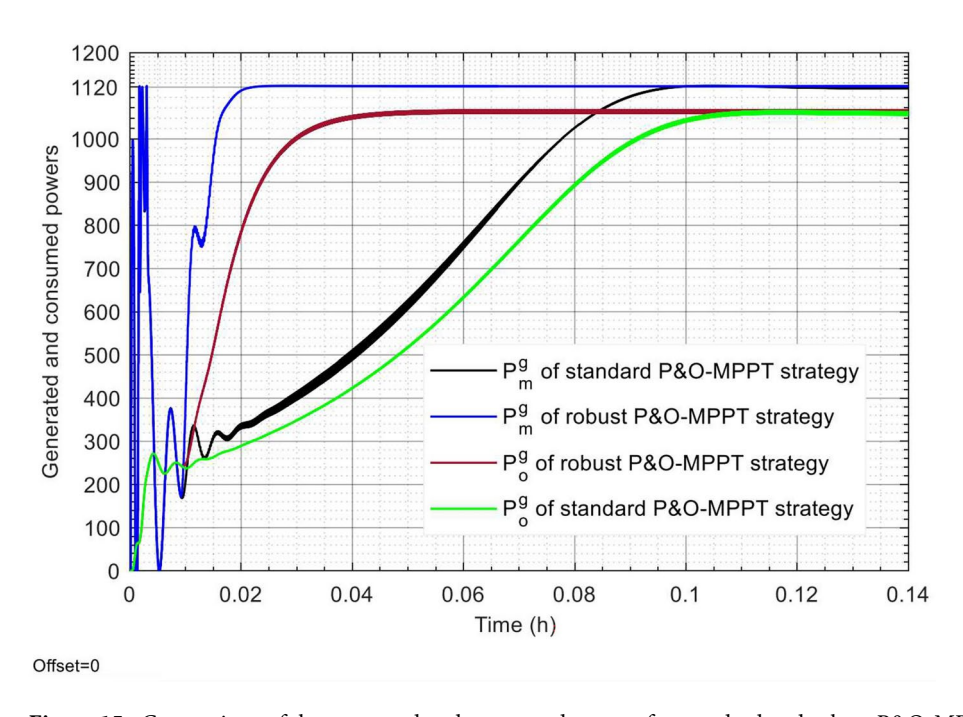


Figure 15. Comparison of the generated and consumed powers for standard and robust P&O-MPPT strategies.

in the initial safety margin resulting from the initial quantification of unstructured relative uncertainties, this new resulting margin can even cover significant variations in this resistive load, even if these variations are not taken into account when developing the RS robustness condition. As a result, the resulting robust controller is always able to maintain the correct balance between performance and robustness, taking into account not only real-time measurements recorded over one day but also those associated with any other unpredictable weather conditions.

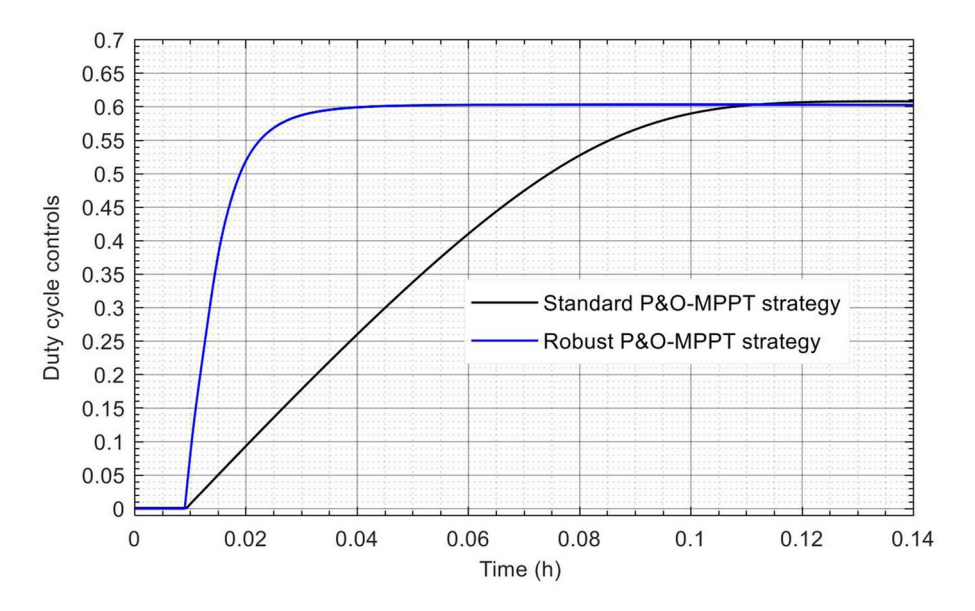


Figure 16. Duty cycle controls generated by standard and robust P&O-MPPT strategies.

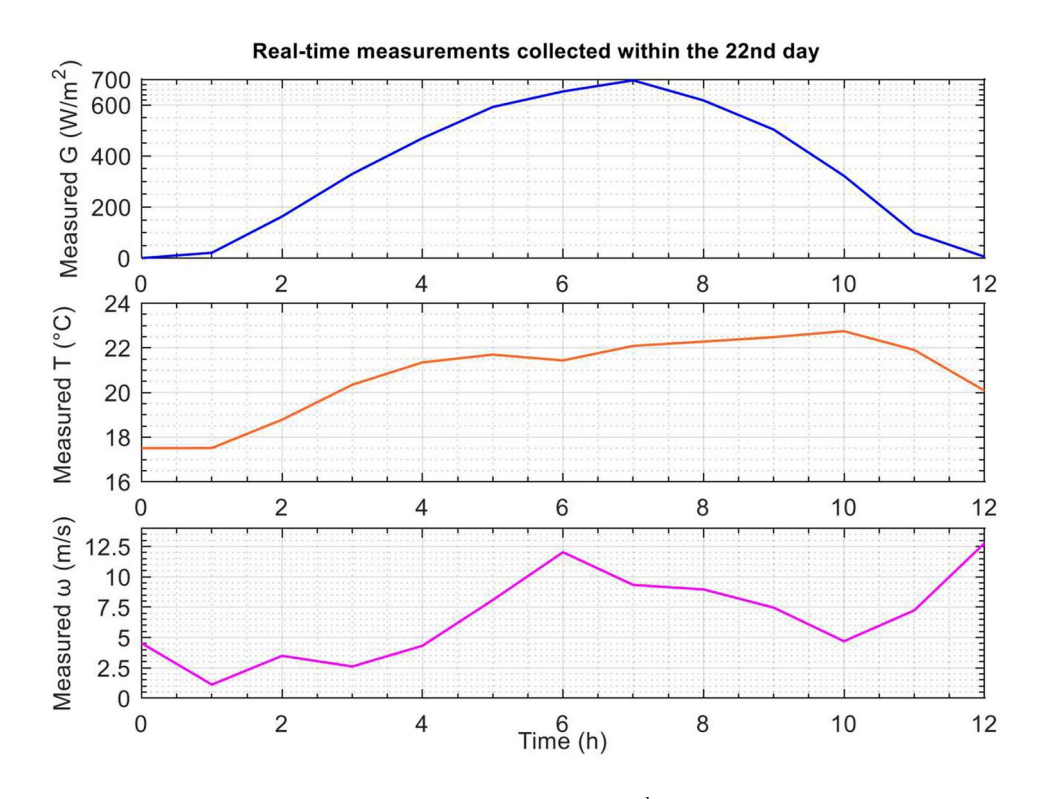


Figure 17. Measured three climatic conditions within the 22^{nd} day of the experimental trial.

Conclusion

In this paper, the design of the new uncertain model describing the actual behavior of the PV array was presented, based on real-time measurements such as outdoor temperature, solar irradiance, and wind speed. The equivalent electrical circuit, incorporating three key parameters, has been developed and their parameters has been optimized using the GA. The resulting uncertain model was then linearized at STC, and the robust H_{∞} controller was synthesized accordingly. This controller was cascaded with the modified Perturb and Observe (P&O) algorithm, resulting in the robust P&O-MPPT strategy. The performance and closed-loop stability of both the standard and proposed P&O-MPPT control strategies were evaluated and compared under STC as well as under varying climatic conditions. Experimental results confirm the effectiveness of the proposed robust P&O-MPPT strategy, which achieves the best tradeoff between reliability and power output under sudden changes in

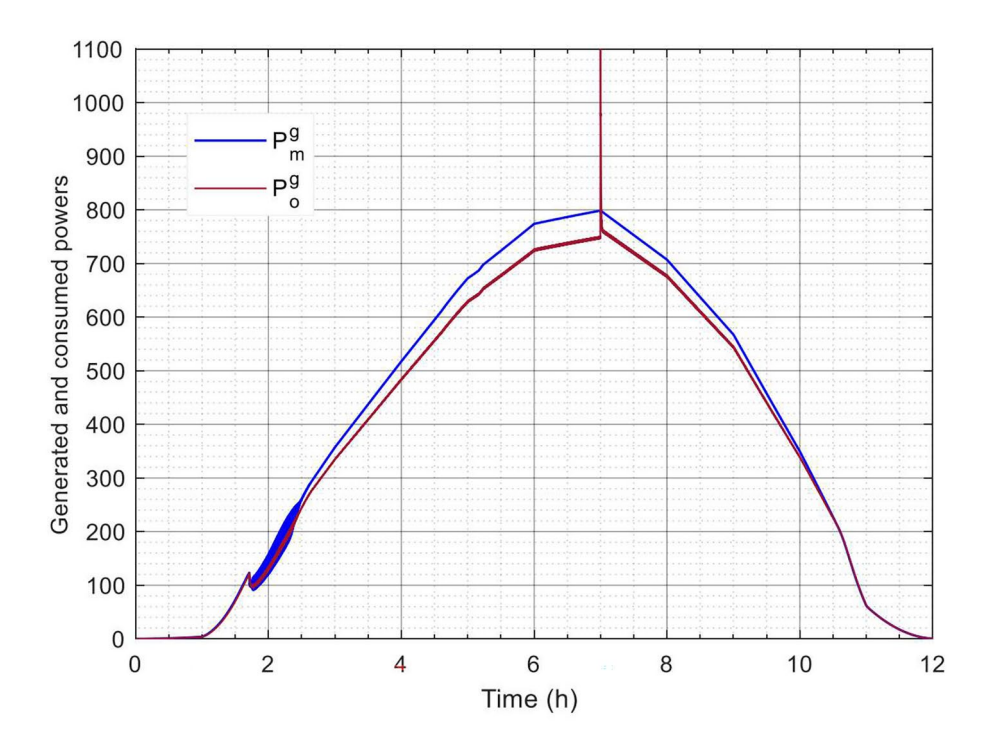


Figure 18. Generated and consumed powers given for 12 hours of one arbitrary day.

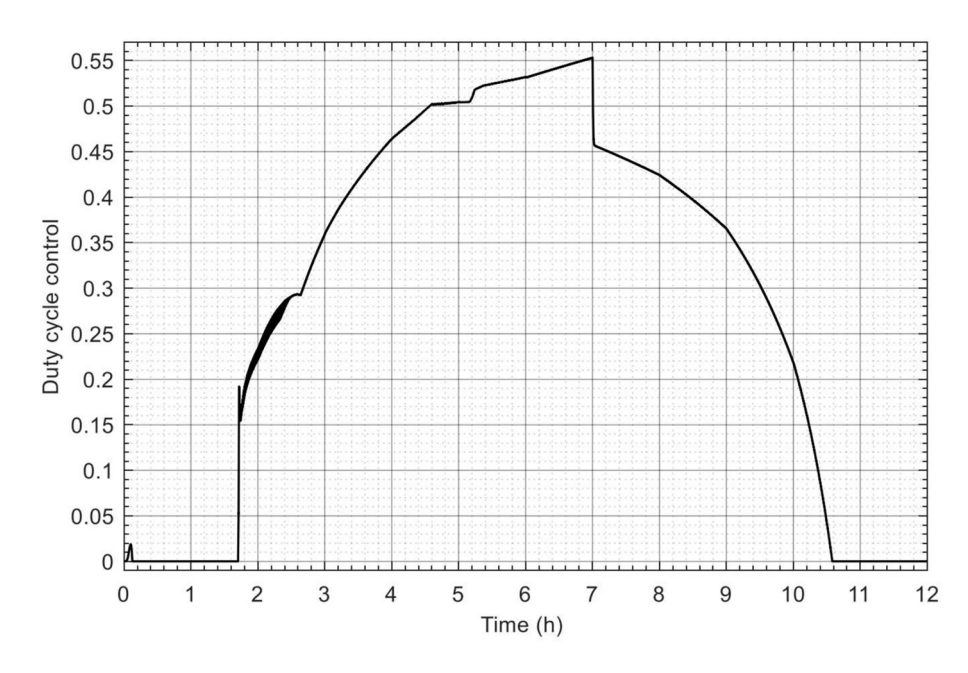


Figure 19. Duty cycle control generated by the fixed-order H_{∞} controller during 12 h of one arbitrary day.

variable load resistance. However, the main limitation of the proposed control strategy arises in its initial stage, where the fixed-size step for updating the reference voltage is chosen manually, which can be problematic when climatic conditions change suddenly. Another limitation is found in the second stage, where other uncertain parameters, especially those related to the DC-DC boost converter, could affect the performance/robustness trade-off. As a suggestion for future research, we recommend to implement a fuzzy logic control law to generate a variable step size for updating the reference voltage. Additionally, we propose the use of self-tuning controller structures that adapt to varying climatic conditions and unpredictable load values.

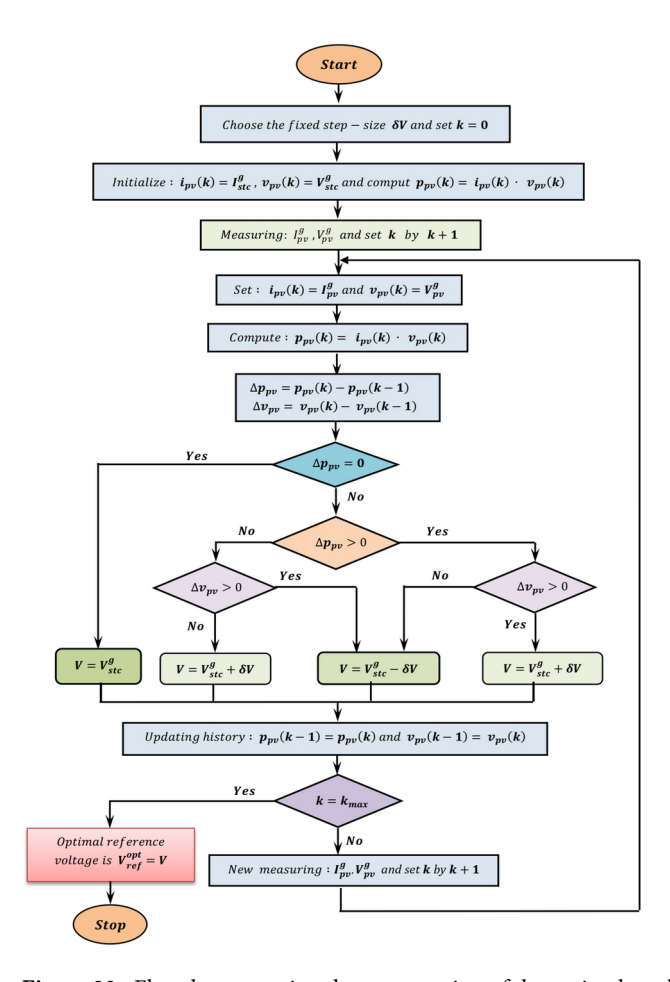


Figure 20. Flowchart ensuring the computation of the optimal total reference voltage.

Data availability

All data generated or analyzed during this study are included in this published article.

Appendix 1

See Fig. 20.

Received: 12 October 2024; Accepted: 10 January 2025

Published online: 23 January 2025

References

- 1. Sehr, M. A. et al. Programmable logic controllers in the context of industry 4.0. IEEE Trans. Ind. Inf. 17, 3523-3533 (2020).
- Afroz, Z., Shafiullah, G., Urmee, T. & Higgins, G. Modeling techniques used in building hvac control systems: A review. Renew. Sustain. Energy Rev. 83, 64–84 (2018).
- 3. Xiao, F., Khammash, M. & Doyle, J. C. Stability and control of biomolecular circuits through structure. In 2021 American Control Conference (ACC), 476–483 (IEEE, 2021).
- 4. Karan, S., Dey, C. & Mukherjee, S. Simple internal model control based modified smith predictor for integrating time delayed processes with real-time verification. *ISA Trans.* 121, 240–257 (2022).
- 5. Guessoum, H., Feraga, C.-E., Mehennaoui, L., Sedraoui, M. & Lachouri, A. A robust performance enhancement of primary h_{∞} controller based on auto-selection of adjustable fractional weights: Application on a permanent magnet synchronous motor. *Trans. Inst. Meas. Control.* 41, 3248–3263 (2019).
- 6. Demirtas, M., Calgan, H., Amieur, T. & Sedraoui, M. Small-signal modeling and robust multi-loop pid and h_{∞} controllers synthesis for a self-excited induction generator. *ISA Trans.* 117, 234–250 (2021).
- 7. Bouarroudj, N. et al. A new tuning rule for stabilized integrator controller to enhance the indirect control of incremental conductance mppt algorithm: Simulation and practical implementation. *Optik* **268**, 169728 (2022).
- 8. Kahla, S. et al. Maximum power extraction framework using robust fractional-order feedback linearization control and gm-cpso for pmsg-based wecs. *Wind Eng.* **45**, 1040–1054 (2021).
- 9. Kollimalla, S. K. & Mishra, M. K. Variable perturbation size adaptive p &o mppt algorithm for sudden changes in irradiance. *IEEE Trans. Sustain. Energy* 5, 718–728 (2014).
- 10. Villalva, M., De Siqueira, T. & Ruppert, E. Voltage regulation of photovoltaic arrays: small-signal analysis and control design. *IET Power Electron.* 3, 869–880 (2010).
- 11. Taibi, D., Amieur, T., Laamayad, T. & Sedraoui, M. Improvement of the standard perturb & observe mppt control strategy by the proposed fuzzy logic mechanism for a cascade regulation of a pmsm-based pv pumping system. *Arab. J. Sci. Eng.* 48, 6631–6647 (2023).

Scientific Reports |

- 12. Aissani, S., Kahla, S., Bechouat, M., Amieur, T. & Sedraoui, M. A voltage pid controller synthesis based on a new small-signal linear model to enhance the performance of the standard p & o algorithm employed in photovoltaic panels. Arab. J. Sci. Eng. 48, 6615-6630 (2023).
- 13. Tadj, M. et al. Enhanced mppt-based fractional-order pid for pv systems using aquila optimizer. Math. Comput. Appl. 28, 99 (2023).
- 14. Refaat, A. et al. Extraction of maximum power from pv system based on horse herd optimization mppt technique under various weather conditions. Renew. Energy 220, 119718 (2024).
- 15. Bechouat, M., Sedraoui, M. & Aissani, S. Improved inc-mppt strategy based on new small-signal design model for solar system using frequency data extracted through graphical interface of plces software. Arab. J. Sci. Eng. 1-14 (2024).
- 16. Motahhir, S., El Hammoumi, A. & El Ghzizal, A. The most used mppt algorithms: Review and the suitable low-cost embedded board for each algorithm. J. Clean. Prod. 246, 118983 (2020).
- 17. Mao, M., Zhang, L., Huang, H., Chong, B. & Zhou, L. Maximum power exploitation for grid-connected pv system under fastvarying solar irradiation levels with modified salp swarm algorithm. J. Clean. Prod. 268, 122158 (2020).
- 18. Kesilmiş, Z., Karabacak, M. A. & Aksoy, M. A novel mppt method based on inflection voltages. J. Clean. Prod. 266, 121473 (2020).
- 19. An, D.-S., Poudel, P., Bae, S.-H., Park, K.-W. & Jang, B. Improved photovoltaic matlab modeling accuracy by adding wind speed effect. J. Chosun Nat. Sci. 10, 58-63 (2017).
- 20. Bechouat, M. et al. Parameters identification of a photovoltaic module in a thermal system using meta-heuristic optimization
- methods. Int. J. Energy Environ. Eng. 8, 331–341 (2017).

 21. Kahla, S., Bechouat, M., Amieur, T., Sedraoui, M. & Guessoum, H. Enhanced the modeling accuracy by the design of new photovoltaic models including the proposed nonlinear thermal resistors. Int. J. Model. Simul. 43, 507-522 (2023).
- 22. Montero-Cassinello, J., Cheah-Mane, M., Prieto-Araujo, E. & Gomis-Bellmunt, O. Small-signal analysis of a fast central control for large scale pv power plants. Int. J. Electr. Power Energy Syst. 141, 108157 (2022).
- 23. Doyle, J. & Stein, G. Multivariable feedback design: Concepts for a classical/modern synthesis. IEEE Trans. Autom. Control 26, 4-16 (1981).
- 24. Skogestad, S., Morari, M. & Doyle, J. C. Robust control of ill-conditioned plants: High-purity distillation. IEEE Trans. Autom. Control 33, 1092-1105 (1988)
- 25. Özbay, H., Smith, M. C. & Tannenbaum, A. Mixed-sensitivity optimization for a class of unstable infinite-dimensional systems. Linear Algebra Appl. 178, 43-83 (1993).
- 26. Oloomi, H. & Shafai, B. Weight selection in mixed sensitivity robust control for improving the sinusoidal tracking performance. In 42nd IEEE International Conference on Decision and Control (IEEE Cat. No. 03CH37475), vol. 1, 300-305 (IEEE, 2003).
- 27. Nair, S. S. Automatic weight selection algorithm for designing h infinity controller for active magnetic bearing. Int. J. Eng. Sci. Technol. 3, 122-138 (2011).
- 28. Gahinet, P. & Apkarian, P. Structured h_{∞} synthesis in matlab. IFAC Proc. Volumes 44, 1435–1440 (2011).
- 29. Ayaz, R., Nakir, I., Tanrioven, M. et al. An improved matlab-simulink model of pv module considering ambient conditions. Int. J. Photoenergy 2014 (2014).
- 30. Saputra, D., Ma'arif, A., Maghfiroh, H., Chotikunnan, P. & Rahmadhia, S. N. Design and application of plc-based speed control for dc motor using pid with identification system and matlab tuner. Int. J. Robot. Control Syst. 3, 233-244 (2023).
- 31. Asadi, F., Pongswatd, S., Eguchi, K. & Trung, N. L. Modeling uncertainties for a buck converter. In Modeling Uncertainties in DC-DC Converters: with MATLAB and PLCES *, 1-62 (Springer, 2019).
- 32. Sedraoui, M., Amieur, T., Bachir Bouiadjra, R. & Sahnoune, M. Robustified fractional-order controller based on adjustable fractional weights for a doubly fed induction generator. Trans. Inst. Meas. Control 39, 660-674 (2017).

Acknowledgements

The authors extend their appreciation to Taif University, Saudi Arabia, for supporting this work through the project number (TU-DSPP-2024-14).

Author contributions

All authors have contributed equally in the preparation of this manuscript.

Funding

This research was funded by Taif University, Taif, Saudi Arabia (TU-DSPP-2024-14).

Declarations

Competing interests

The authors declare no competing interests.

Ethical approval

This article does not contain any studies with human participants or animals performed by any of the authors.

Additional information

Correspondence and requests for materials should be addressed to M.S. or Y.A.A.

Reprints and permissions information is available at www.nature.com/reprints.

Publisher's note Springer Nature remains neutral with regard to jurisdictional claims in published maps and institutional affiliations.

Open Access This article is licensed under a Creative Commons Attribution-NonCommercial-NoDerivatives 4.0 International License, which permits any non-commercial use, sharing, distribution and reproduction in any medium or format, as long as you give appropriate credit to the original author(s) and the source, provide a link to the Creative Commons licence, and indicate if you modified the licensed material. You do not have permission under this licence to share adapted material derived from this article or parts of it. The images or other third party material in this article are included in the article's Creative Commons licence, unless indicated otherwise in a credit line to the material. If material is not included in the article's Creative Commons licence and your intended use is not permitted by statutory regulation or exceeds the permitted use, you will need to obtain permission directly from the copyright holder. To view a copy of this licence, visit http://creativecommons.org/licenses/by-nc-nd/4.0/.

© The Author(s) 2025